Thesis for a Ph. D. Degree

Retrieval of wintertime snow depth on Arctic sea ice and analysis of long-term variability using satellite passive measurements

인공위성 수동 관측자료를 활용한 겨울철 북극 해빙지역 적설깊이 산출 및 장기변동성 분석

August 2021

School of Earth and Environmental Sciences

Graduate School

Seoul National University

Hoyeon Shi

Retrieval of wintertime snow depth on Arctic sea ice and analysis of long-term variability using satellite passive measurements

By

Hoyeon Shi

A dissertation submitted to the faculty of the graduate school of the Seoul National University in partial fulfillment of the requirements for the Degree of Doctor of Philosophy

Degree Awarded:

August 2021

Advisory committee:

Professor Kwang-Yul Kim, Chair

Professor Byung-Ju Sohn, Advisor

Professor Sang-Woo Kim

Doctor Hyun-Cheol Kim

Professor Young-Ho Kim

Retrieval of wintertime snow depth on Arctic sea ice and analysis of long-term variability using satellite passive measurements

인공위성 수동 관측자료를 활용한 겨울철 북극 해빙지역 적설깊이 산출 및 장기변동성 분석

지도교수 손 병 주

이 논문을 이학박사 학위논문으로 제출함
2021년 5월

서울대학교 대학원
지구환경과학부
시 호 연

시호연의 이학박사 학위논문을 인준함
2021년 7월

위 원 장 _____

부위원장 _____

위 원 _____

위 원 _____

위 원 _____

Abstract

A new satellite retrieval algorithm for wintertime snow depth on Arctic sea ice was developed based on the hydrostatic balance and thermodynamic steady-state of a snow-ice system. In this algorithm, snow depth is estimated from the passive infrared and microwave measurements, with the use of sea ice freeboard, snow surface temperature, and snow-ice interface temperature as inputs. The algorithm was validated against NASA's Operation IceBridge (OIB) measurements, and results indicate that the snow depth on the Arctic sea ice can be estimated with a high level of accuracy. To produce a long-term snow depth record in the Arctic basin-scale, sea ice freeboard was estimated from the satellite passive microwave (PMW) measurements. To do so, the snow-ice scattering optical depth from satellite PMW measurements was used as a predictor for the estimation of the total freeboard. Estimated PMW total freeboards were found to be in good agreement with OIB total freeboards.

The wintertime snow depth records for the 2003-2020 period were produced by combining the PMW freeboard and satellite-derived temperatures. It was found that snow depth is highly dependent on sea ice type, likely due to the snow accumulation timing and period. The snow depth and its variability were greater on multiyear ice than on first-year ice. Besides, a significant reduction in mean snow depth was found, compared to the snow depth climatology for the 1954-1991

period. Regarding the temporal variations over the 2003-2020 period, regionally different snow depth trends are found; negative and positive snow depth trends were noted over the eastern and western parts of the Arctic Ocean, respectively. It is thought that the negative trends are related to sea ice type transition and delayed freeze onset, while the positive trends are related to increased precipitation amount.

Keywords: Snow depth, Arctic sea ice, Satellite Remote Sensing, Climate Change

Student number: 2016-29111

Table of Contents

List of Tables

List of Figures

1. Introduction

Arctic sea ice is frozen sea water that covers the Arctic Ocean enclosed by Eurasian and North American continents. Sea ice plays important role in the Arctic climate system. Sea ice, generally covered with snow layer, is one of the brightest materials on Earth's surface with high reflectivity. Thus, much of the insolation reaching the sea ice is reflected into space during the melting period (e.g., a period from spring to fall when sunlight is present in the Arctic region). As a result, surfaces covered by sea ice absorb less solar energy, so temperatures in the Arctic regions remain relatively cool. Sea ice is also related to meridional ocean circulation. When sea ice forms, salt dissolved in sea water is discharged into the water below the ice. This phenomenon makes sea water below sea ice denser than the surroundings. As a result, cold and dense polar water sinks and moves toward the equator, while warm water moves from the equator toward the Arctic Ocean. This meridional circulation is as known as ‘Atlantic meridional overturning circulation’.

The coverage of Arctic sea ice has an annual cycle. It reaches a maximum in spring when solar insolation starts to affect the Arctic Ocean and reaches a minimum in fall when sea ice melting terminates, and new ice formation starts. Sea ice starts to form when the temperature of sea water reaches the freezing

temperature that is approximately -1.8°C. The freezing temperature of sea water is lower than that of fresh water because sea water is saline. There are mainly two ways in the sea ice growth process. One way is thermodynamic growth. During the freezing period, cold atmosphere uptakes the thermal energy from the ocean through sea ice. As a result, sea ice growth takes place at the ice bottom, where the ocean loses thermal energy. Consequently, the temperature at the ice bottom remains at an almost constant value because phase transition (i.e., freezing) takes place at the ice bottom. The other way of sea ice growth is dynamic growth. Sea ice floating on the Arctic Ocean does not stay at one location, but it moves around the Arctic Ocean due to external forces such as wind and ocean currents. Due to the mobility of sea ice, the convergence of ice floes can occur. Sea ice can grow by this convergence forming surface features such as pressure ridges. Similarly, sea ice loss can occur by melting due to warm temperature and break up due to divergence.

Due to global warming, Arctic sea ice cover is decreasing rapidly (Andersen et al., 2020). A warm Arctic environment makes sea ice more vulnerable to external perturbations. Tinner ice is much more likely to melt away during summer than thicker ice because less energy is required to melt thinner ice. Moreover, thinner sea ice is prone to break up into small ice floes with greater mobility due to ocean waves and winds. The increased mobility of sea ice makes sea ice easier

to be exported from the Arctic Ocean to the lower latitude region by transpolar drift. It is reported that the change in intensified atmospheric circulation such as Arctic Oscillation can significantly remove Arctic sea ice by sea ice export through Fram straight (Rigor and Wallace, 2004). In this situation, the portion of multiyear ice (MYI) which survived the summer melting period decreases rapidly, and the dominant wintertime ice type now becomes first-year ice (FYI) which is newly formed sea ice.

While diminishing Arctic sea ice has become the most vivid evidence of global warming, the sea ice loss is not only the consequence of global warming but also the driver of accelerated Arctic warming. If sea ice area with high albedo decreases, the solar energy absorbed by the surface increases. As a result, the surface warming and the sea ice loss forms a positive feedback loop as known as 'albedo feedback'. The rate of Arctic temperature rise is more than twice the global warming rate, which is called Arctic amplification (Serreze and Barry, 2011; Screen and Simmonds, 2010). The impact of the Arctic amplification extends to the midlatitude region by providing favorable conditions for the wavier jet (Francis and Vavrus, 2015). It is thought that the wavier jet during winter is closely related to the East Asian cold surge (Kug et al., 2015).

Heretofore, studies on the role of sea ice in weather and climate have been focused on the sea ice cover of which the Arctic basin-scale data are continuously

available from satellite passive microwave (PMW) measurements for more than 30 years. However, sea ice thickness is as important as sea ice cover because the degree of insulation effect (i.e., reducing energy transport between atmosphere and ocean) depends on the sea ice thickness. A modeling study showed that the Arctic amplification factor has increased 37% when sea ice thickness change was involved in calculation compared to when fixed ice thickness was used (Lang et al., 2017). However, the aforementioned study did not consider the change of snow depth on sea ice. Considering that snow is a great insulator with very low thermal conductivity compared to sea ice (Maykut and Untersteiner, 1971; Sturm et al., 1997; Sturm et al., 2002), the effect of snow depth change should be included to derive a more solid conclusion.

Especially, snow depth on sea ice is necessary information for estimating sea ice thickness from satellite altimeter observations. The altimeters do not measure sea ice thickness directly but measure sea ice freeboard (i.e., height from a local sea surface to snow or ice surface). Once the freeboard measurement is available, a buoyancy equation is applied to covert freeboard to sea ice thickness with the assumption that input parameters such as snow depth, the snow and ice densities, and the radar penetration depth are known (Ricker et al., 2014). The buoyancy equation describes the balance between the buoyant force and the weight of snow and ice, and thus the sea ice thickness is a function of snow depth for a given sea

ice freeboard and densities. Furthermore, the conversion results are highly dependent on snow depth (Kern et al., 2015; Ricker et al., 2014; Zygmuntowska et al., 2014, Kim et al., 2020). Therefore, obtaining the spatial distribution of snow depth is a very crucial issue for sea ice thickness estimation.

Fundamental knowledge on snow depth was achieved by the monumental work of Warren et al. (1999) (hereafter referred to as W99) which constructed monthly snow depth climatology fields from extensive in-situ measurements during the 1954-1991 period. However, it has been reported that recent snow depth has been reduced significantly compared to the W99 snow depth climatology (Webster et al., 2014; Kurtz and Farrell, 2011). Therefore, the use of W99 for a recent period may induce more uncertainty in retrieving the sea ice thickness. There are other in-situ snow depth measurements from the ongoing Arctic buoy program such as the Cold Regions Research and Engineering Laboratory – Ice Mass Balance (CRREL-IMB) buoy program (Perovich et al., 2019), and Alfred Wegener Institute (AWI) buoy program (Grosfeld et al., 2016). Nevertheless, those point measurements cannot capture snow depth distribution over the whole Arctic Ocean. Even if the new climatology is constructed in a similar way to W99, great interannual variability of snow depth cannot be treated. Therefore, Arctic basin-scale snow depth observations are highly desirable.

There have been various approaches aimed at estimating the snow depth distribution using satellite PMW observations. Markus and Cavalieri (1998) developed an algorithm based on the Brightness Temperatures (TBs) of Special Sensor Microwave/Imager (SSM/I) based on the negative correlation of the snow depth with the spectral gradient ratio (GR) between 18 and 37 GHz of vertically polarized TBs, but only on the Antarctic FYI. Comiso et al. (2003) have updated the coefficients of this algorithm for the Advanced Microwave Scanning Radiometer for EOS (AMSR-E). However, snow depth retrieval using this algorithm is reported to be less accurate when the MYI fraction within the grid cell is significant (Brucker and Markus, 2013). Recently, Rostosky et al. (2018) suggested a new method using the lower frequency pair of 7 and 19 GHz to overcome such limitation – for the time being this lower frequency algorithm is valid only for March and April months over the MYI region.

There are other approaches involving the use of the lower frequency measurements at the L-band. Using Soil Moisture Ocean Salinity (SMOS) measurements, Maaß et al. (2013) found that 1.4 GHz TB has a dependence on the snow depth because of the insulation effect of the snow layer, and they determined snow depth by matching Radiative Transfer Model (RTM) simulated TBs with SMOS-measured TBs. Zhou et al. (2018) simultaneously estimated the sea ice thickness and snow depth by adding additional lidar altimeter freeboard

information, improving the Maaß et al. (2013) approach. However, both RTM-based approaches require a priori information on ice properties (e.g., temperature and salinity profiles). Other satellite remote sensing approaches include the snow depth retrieval using dual-frequency altimetry (Guerreiro et al., 2016; Lawrence et al., 2018; Kwok et al., 2020), multilinear regression (Kilic et al., 2019), and a neural network approach (Braakmann-Folgmann and Donlon, 2019). Nonetheless, estimating the basin-scale snow depth distribution seems so far to be a difficult task. More detailed reviews on previous approaches to obtain snow depth information can be found in Section 2.

Here, instead of retrieving the snow depth directly, let us switch our point of view to finding a constraint that can be used for snow depth retrieval. There are two unknowns (i.e., snow depth and ice thickness) in the buoyancy equation for a given freeboard. If a particular relationship between snow depth and ice thickness exists, it may be possible to constrain the buoyancy equation to solve simultaneously both ice thickness and snow depth.

To find a possible relationship between snow depth and ice thickness, this study examines the vertical thermal structure within the snow-ice system. The wintertime vertical temperature profile of the snow–ice system can be assumed to be piecewise linear, as illustrated in Figure 1. Therefore, the temperatures at three interfaces can describe the thermal structure of the snow-ice system fairly well;

they are (1) air–snow interface temperature (T_{as}), (2) snow–ice interface temperature (T_{si}), and (3) ice–water interface temperature (T_{iw}). T_{iw} is assumed to be nearly constant at the freezing temperature of seawater, implying that two other interface temperatures (T_{as} and T_{si}) may be enough to describe the thermal structure of the system. Therefore, the thermal structure of a snow-ice system can be resolved from satellite observations of T_{as} (Dybkjær et al., 2014) and T_{si} (Lee et al., 2015) in the Arctic basin-scale.

Based on the assumption on the thermal structure, we attempt to find a relationship between the snow depth and ice thickness which can be used as a constraint for reducing the unknown variables in the hydrostatic balance equation. Identifying the relationship, conductive heat flux is assumed to be continuous through the snow–ice interface (Maykut and Untersteiner, 1971), implying that conductive heat fluxes within the snow and ice layers are the same under the steady-state. Considering that the conductive heat flux is proportional to the bulk temperature difference of a layer divided by the thickness of the corresponding layer, it is possible to deduce the ratio between snow depth and ice thickness (hereafter referred to as thickness ratio; *TR*) under the given steady-state. *TR* can be used with freeboard measurements to yield snow depth and sea ice thickness simultaneously.

Meanwhile, a recent study by Lee et al. (2021) showed that it is possible to estimate ice freeboard from satellite PMW measurements by relating snow-ice scattering optical depth (SOD) due to snow and freeboard scatterings with ice freeboard. As PMW freeboard from AMSR measurements can provide consistent freeboard record for January-February-March (JFM) months during the 2003-2020 period, it is suitable for constructing a long-term snow depth record, synergized with the *TR*. Based on this background, this study aims to accomplish the followings:

(1) Develop a snow depth retrieval algorithm based on the vertical thermal structure of a snow-ice system and freeboard measurements during wintertime.

(2) Construct snow depth record for JFM months during the 2003-2020 period by using the developed retrieval algorithm in combination with PMW-derived freeboards.

(3) Examine the geographical distribution and temporal variations of snow depth for the 2003-2020 period with related geophysical processes.

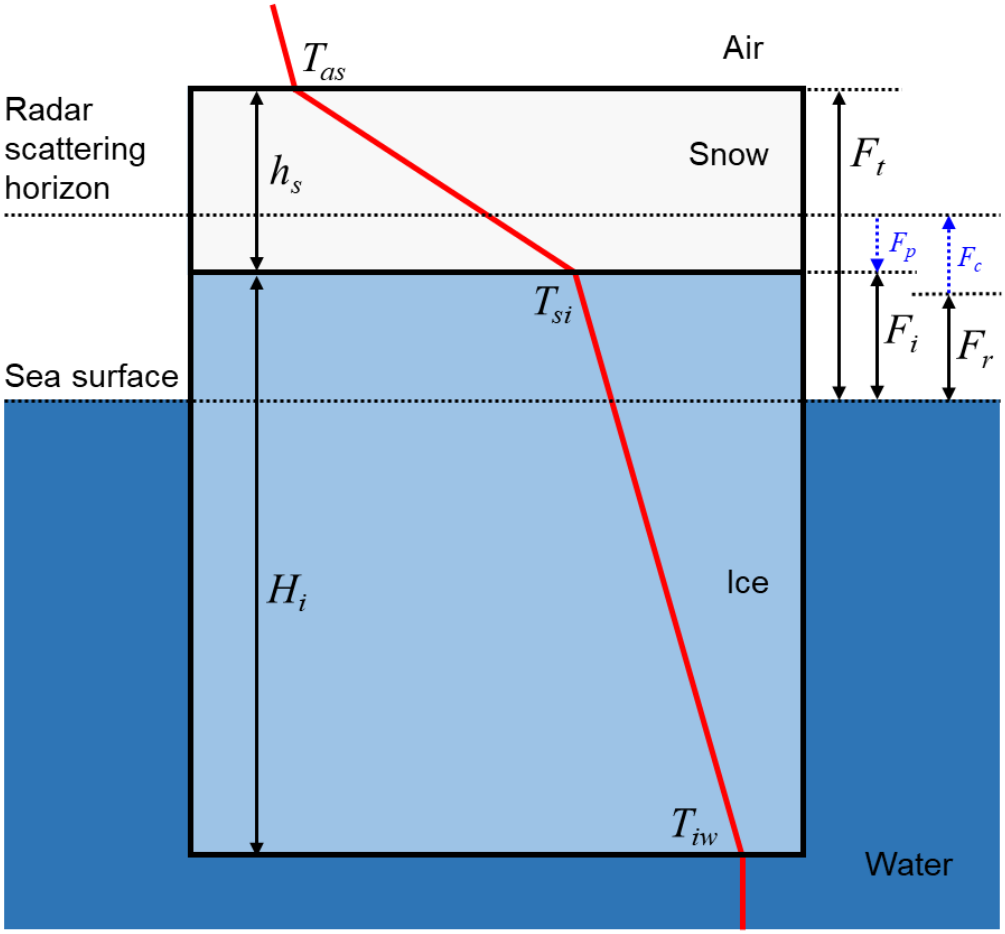

Figure 1. Schematic diagram of a typical snow–ice system during the winter. Snow depth (h_s), ice thickness (H_i), total freeboard (F_t), radar freeboard (F_r), and ice freeboard (F_i) are indicated. Correction terms regarding the wave propagation speed change in the snow layer (F_c) and the displacement of the scattering horizon from the ice surface (F_p) are indicated by blue arrows. The red line denotes a typical temperature profile with air–snow interface temperature (T_{as}), snow–ice interface temperature (T_{si}), and ice–water interface temperature (T_{iw}).

2. Previous studies in obtaining Arctic snow depth

2.1. In situ measurements

2.1.1. Snow depth climatology

Although the Arctic ocean is a severe environment for humans to reach, there have been pioneers who endeavored to obtain in situ measurements of snow depth. Soviet Union operated many manned stations established on the drifting MYI over the Central Arctic Ocean to conduct in situ measurements of ocean and atmosphere including snow depth. Those stations are called 'North Pole (NP) stations' and the spatial and temporal coverage of the stations are presented in Figure 2a. Warren and his colleagues produced the monthly snow depth climatology based on the snow depth measured at NP stations during the 1954 to 1991 period. Snow depth climatology was produced by fitting a two-dimensional quadratic function to the massive snow depth measurements. The snow depth climatology for January month is shown in Figure 2b.

In addition, there was an airborne expedition conducted by the Soviet Union during the 1959-1988 period. The name of the expedition is 'Sever' which is the Russian word for 'north'. During the spring season, skilled personnel landed on Arctic sea ice including both FYI and MYI, and measured sea ice parameters such as snow depth, snow density, and ice thickness. The data obtained from the Sever

expedition can be found at the National Snow and Ice Data Center (NSIDC) website (https://doi.org/10.7265/N5B8562T). As the spatial coverage and number of measurements of the Sever expedition are much wider and greater than that of NP stations, particularly in the Eurasian marginal seas (Figure 3a and 3b), Shalina and Sandven (2018) analyzed snow depth data from Sever expeditions to produce updated snow depth climatology (Figure 3c).

Because of difficulties in the estimation of the Arctic basin-scale snow depth, these snow depth climatological values are still considered as a standard reference. However, as the climate in the Arctic region changes rapidly, it is difficult to accept that this snow depth climatology is a representative value for the recent periods.

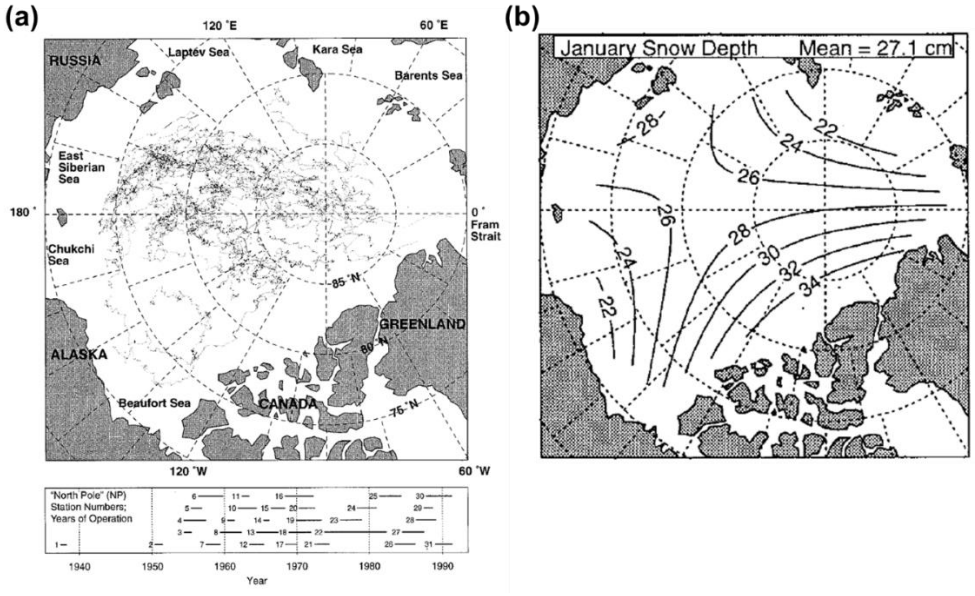

Figure 2. (a) Paths of NP drifting stations and years of operation of each drifting station. (b) Obtained snow depth climatology for January. (Figures from Warren et al., 1999)

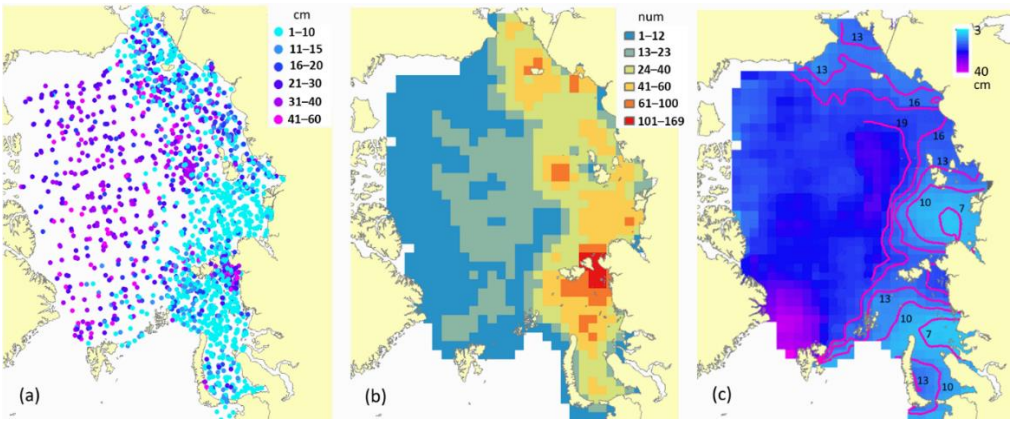

Figure 3. (a) Geographical distributions of snow depth measurement sites for March-April-May months during the 1959–1988 period. (b) The number of measurements within gridded area of 100 × 100 km. (c) Contours of the snow depth obtained from observations shown in (a) (Figure from Shalina and Sandven, 2018)

2.1.2. Arctic buoy programs

In recent days, it is almost impossible to conduct massive, labor-intensive, and dangerous expeditions for the Arctic Ocean in situ measurements. Instead, automated in situ measurements are carried out by installing observation devices on the sea ice and using it as a buoy as illustrated in Figure 4. Once the buoys are deployed, measurements of sea ice parameters such as ice thickness, snow depth, temperature profile are made along the drift track of sea ice floe. One of the most famous Arctic buoy programs is the Ice Mass Balance (IMB) buoy program operated by Cold Regions Research and Engineering Laboratory (CRREL) in the United States. The CRREL-IMB buoy data are available from 2000 to the present at the CRREL website (http://imb-crrel-dartmouth.org/). Other buoy data are available from the Surface Heat Energy Budget of the Arctic (SHEBA) campaign (Perovich et al., 2007) and Alfred Wegener Institute (AWI) buoy program (Grosfeld et al., 2016). These buoy data are widely used as a training dataset for satellite retrieval algorithm development or validation dataset.

However, special cautions should be made for the usage of these buoy data. Because buoy observation is autonomous, the measurement setting cannot be controlled perfectly even if it was perfect when it was initially installed. For example, accurate observation may fail due to the tilting of the device. In the case of snow depth measurements, it utilizes an acoustic sounder which must be

installed perpendicular to the surface for accurate ranging. Besides, buoy data are point measurements that may not be representative of the area around the buoy. Therefore, direct comparison between the buoy and satellite data may not appropriate for the variable with high spatial inhomogeneity.

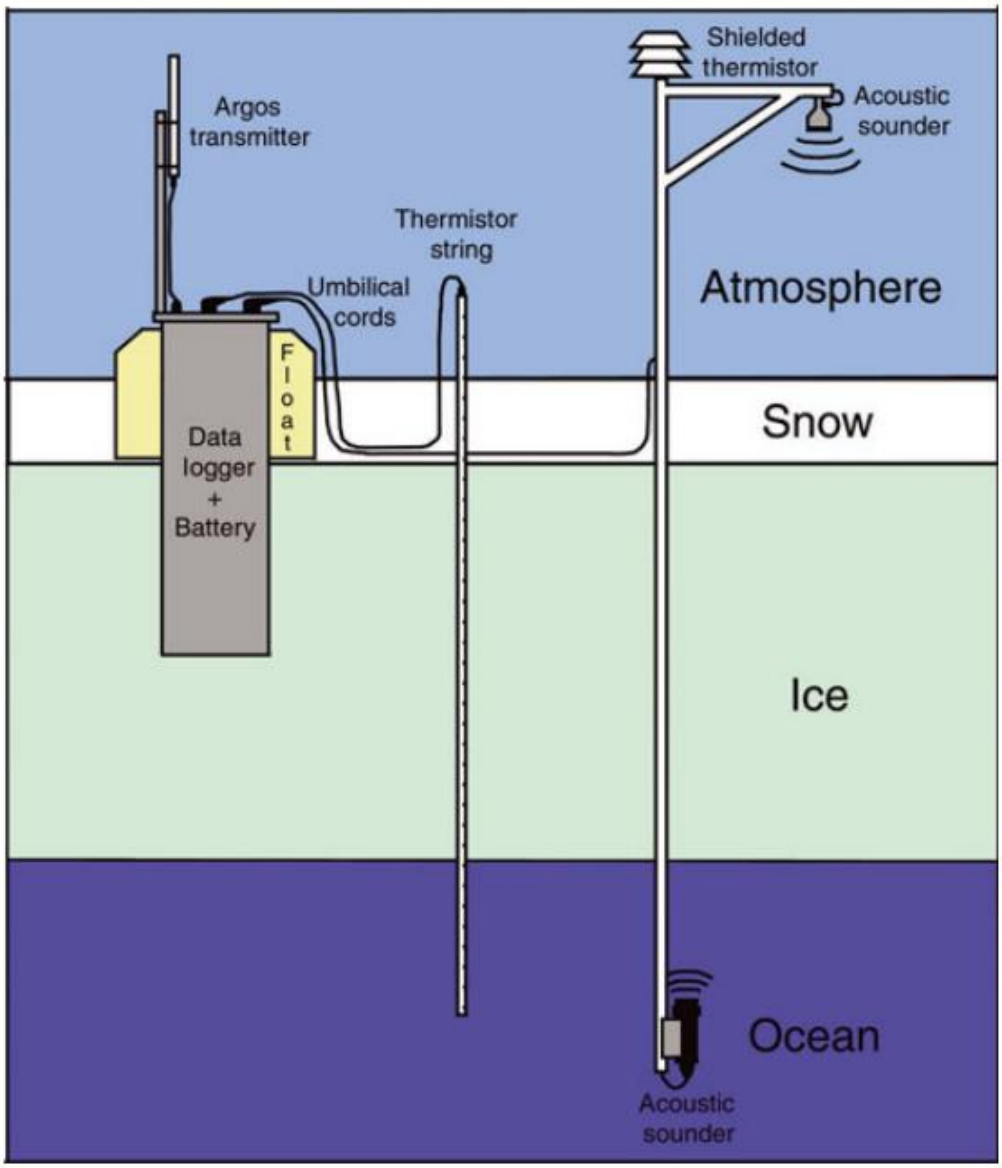

Figure 4. Schematic diagram of an ice mass-balance buoy (Figure from Polashenski et al., 2011)

2.2. Remote sensing

2.2.1. Operation IceBridge

To overcome the harsh environment of the Arctic Ocean, observations of Arctic sea ice are also done with remote sensing approaches. One of the most famous and widely used remote sensing datasets is from NASA's Operation IceBridge (OIB) which is an airborne mission. The main objective of the OIB mission is to extend and improve the record of sea ice observations begun by ICESat which terminated its operation in 2008 (Zwally et al., 2002). This mission was terminated in 2019 as ICESat-2 (Markus et al., 2017) is launched and become operational.

OIB utilizes a highly specialized aircraft equipped with various sensors. Those are high resolution visible digital camera for surface mapping (Digital Mapping System; DMS), lidar altimeter for surface height estimation (Airborne Topographic Mapper; ATM), infrared radiometer for surface temperature estimation (KT-19), ultra-wideband snow radar for snow depth estimation, etc. (Figure 5a). OIB generally collects snow and ice data only for the western part of the Arctic Ocean (Figure 5b). Since OIB data have relatively high accuracy among other remotely sensed data with a more comparable spatial scale to satellite measurements, it is mainly used as a validation dataset in the field of satellite

remote sensing. However, airborne measurements are available for the spring season (i.e., March, and April) because flight without sunlight during the Arctic winter season is dangerous.

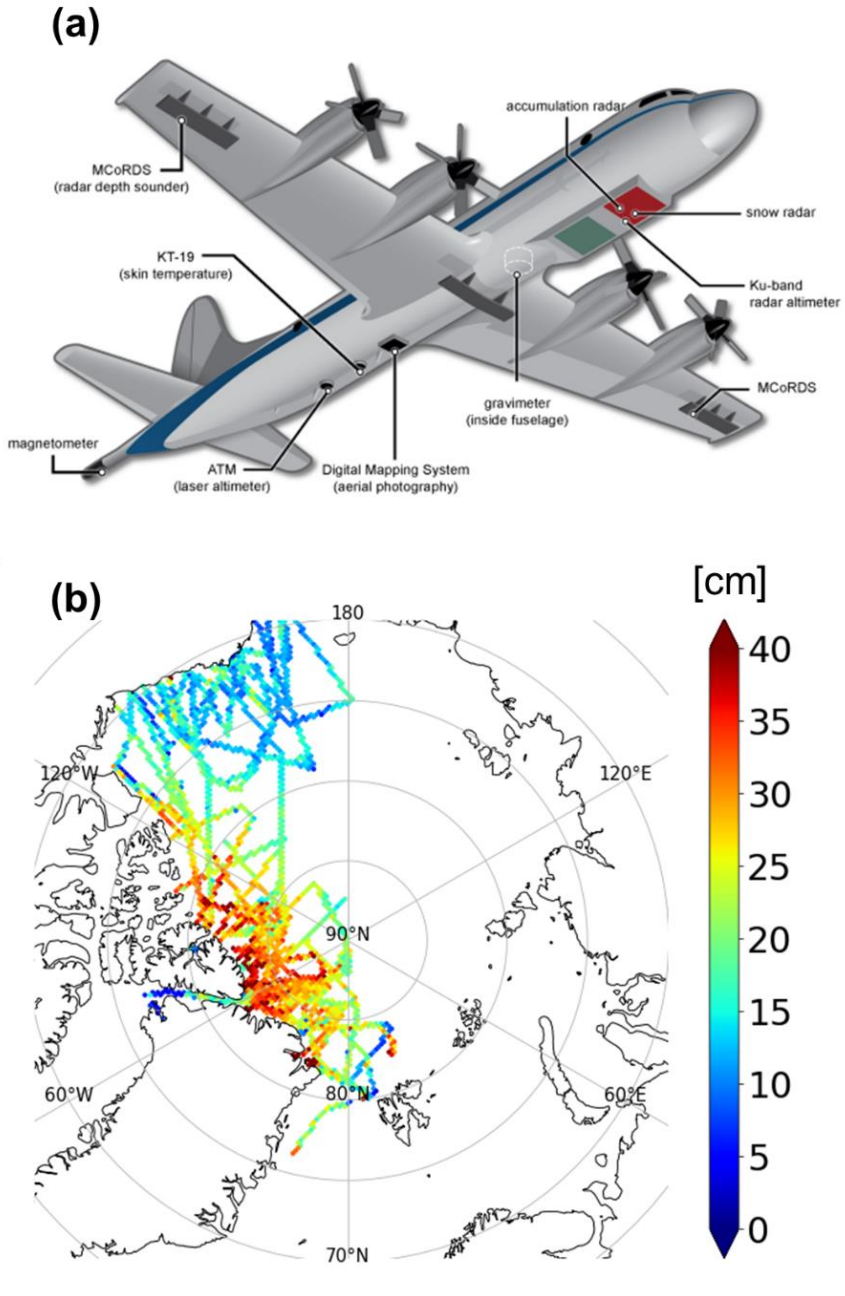

Figure 5. (a) Measurement devices equipped in airplane used for OIB mission (image from OIB website; https://icebridge.gsfc.nasa.gov/). (b) Mean OIB snow depth for March month for the 2010-2018 period.

2.2.2. Satellite passive microwave (PMW) measurements

Many studies utilize satellite PMW measurements to estimate Arctic basin-scale snow depth, advantaged by the low sensitivity of microwave signal to hydrometeor and water vapor. Markus and Cavalieri (1998) found that GR (i.e., a normalized difference of TBs at two different frequencies) between 18 and 37 GHz of vertically polarized TBs are negatively correlated with snow depth on Antarctic FYI by comparing SSM/I and in situ measurements. This phenomenon is due to the radiometric nature that the TBs at higher frequencies are more likely to be attenuated by the snow layer scattering than TBs at lower frequencies.

Based on their findings, Comiso et al. (2003) made a snow depth retrieval algorithm for Arctic FYI using AMSR-E measurements. However, this GR-based algorithm does not work for thick snow on MYI because the difference in TB is saturated. Recently, Rostosky et al. (2018) suggested a new method using GR from the lower frequency pair of 7 and 19 GHz to overcome that limitation. They regressed the GR values from AMSR2 measurements with OIB snow depth to obtain the snow depth prediction equation, separately for FYI and MYI. The validation results showed fair accuracy, however, this lower frequency algorithm is valid only for March and April months when OIB training data are available.

There is an approach using the PMW measurements at the L-band. Maaß et al. (2013) found that 1.4 GHz TB has a dependence on the snow depth. Theoretically, the snow layer is almost transparent at L-band, thus this dependency was not able to be explained by radiative transfer knowledge. It was found that this phenomenon was due to the insulation effect of the snow layer: a thicker snow layer makes ice temperature warmer. Based on this, Maaß et al. (2013) determined snow depth by matching RTM simulated TBs and SMOS-measured TBs. However, the inclusion of RTM requires a priori information on ice properties such as temperature and salinity profiles.

In addition, advanced statistical algorithms have been developed. Kilic et al. (2019) performed multivariate linear regression analysis using the AMSR2 TBs and snow depth measurements from buoy observations. Besides, Braakmann-Folgmann and Donlon (2019) used GR values for three different frequency pairs from AMSR2 measurements as a predictor for snow depth estimation. They trained an artificial neural network with those variables with OIB snow depth. Both the methods show better accuracy than the previous methods, however, there may be an overfitting problem with advanced statistics-based algorithms. In other words, accuracy is not guaranteed for the data not included in the training set.

2.2.3. Dual-frequency satellite altimetry

Snow depth can be estimated from satellite altimeter measurements and the fundamental principle of this approach is very simple and robust. Reminding that snow depth is a distance from the snow-ice interface to the snow surface, snow depth estimation can be estimated from the height of the snow-ice interface and the height of the snow surface. That information can be obtained by satellite altimeter measurements. Satellite altimeter emits electromagnetic wave to surface and receives the surface reflected wave. The satellite altimeter measures the travel time of the wave which provides information on the distance from the reflecting surface to the satellite. An electromagnetic wave with a higher frequency (shorter wavelength) is reflected at the snow surface, while the wave with a lower frequency (longer wavelength) penetrates the snow layer and is reflected near the snow-ice interface. Therefore, snow depth can be estimated from satellite altimeter measurements at two different frequencies. Based on this, Kwok et al. (2020) estimated snow depth using ICESat-2 which is a lidar altimeter, and CryoSat-2 which is a radar altimeter. However, overlapping of the two altimeters are available since 2018, thus this method cannot provide past snow depth records.

3. Used data

3.1. Snow-ice temperature profiles

In-situ measurements of temperature profile within the snow and ice layers are used to obtain the relation between *TR* (defined in the introduction) and vertical thermal structure of the snow-ice system (hereafter referred to as *TR*-temperature equation). These temperature profiles are obtained by thermistor chain implanted into the ice floe, as parts of the buoys deployed over the Arctic ocean for the AWI buoy program (Grosfeld et al., 2016). The buoy measurements are used for further analysis if temperature records are continuously available from December of the year when the buoy was deployed, to the following March. Data showing bad quality (e.g., spiky-shaped temperature profiles or GPS positions holding sudden jumps to a very distant place) are subjectively filtered out. Detailed information on the ice type and initial snow/ice thickness at buoy deployment locations is provided in Table 1.

Table 1. Information on the measurement sites of AWI buoys whose observations were used in this study.

Buoy name	Deployment location	Ice type	Initial snow depth (m)	Initial ice thickness (m)
2014T14	81.93°N, 131.13°E	Multi-Year	0.07	1.49
2014T33	89.97°N, 29.64°E	Multi-Year	0.11	2.22
2015T25	88.34°N, 144.32°W	First-Year	0.15	1.45
2018T46	80.44°N, 161.93°E	Multi-Year	0.004	1.82
2018T52	80.96°N, 163.18°E	Multi-Year	0	2.39
2018T54	79.17°N, 167.97°E	Multi-Year	0	2.62
2018T55	80.72°N, 159.83°E	Multi-Year	0.003	2.11
2019T56	85.83°N, 122.46°E	-	-	-
2019T58	85.11°N, 136.20°E	-	0.1	1.57
2019T62	85.65°N, 125.47°E	-	-	-
2019T63	85.00°N, 135.00°E	-	0.1	1.06
2019T64	85.13°N, 133.17°E	-	0.14	1.74
2019T65	85.00°N, 135.03°E	-	0.15	1.31
2019T66	85.65°N, 125.51°E	-	-	-
2019T67	85.01°N, 132.78°E	-	0.13	1.44
2019T68	84.92°N, 131.26°E	-	0.15	1.8
2019T70	85.13°N, 135.68°E	-	0.06	0.45
2019T72	85.05°N, 139.02°E	-	0.13	0.97

3.2. Satellite data

3.2.1. PMW brightness temperature

To retrieve T_{si} (Lee et al., 2015), SOD (Lee et al., 2021), and sea ice type (Lee et al., 2017), Level-3 daily TB fields from AMSR-E and AMSR2 at 6.925, 10.65, 18.5, and 36.5 GHz for JFM months of 2003-2020 are used. Ascending and descending TB fields are averaged to obtain daily TB fields. Data are provided in a 25 km polar stereographic grid format by Japan Aerospace Exploration Agency (JAXA) through their G-portal (ftp.gportal.jaxa.jp). There is a data gap in 2012 because AMSR was not operational.

Atmospheric correction is done by using Satellite Data Simulator Unit (SDSU)-version 2.1 (Masunaga et al., 2010) with inputs from the European Centre for Medium-Range Weather Forecast (ECMWF) ReAnalysis-5th Generation (ERA5; Hersbach et al., 2020). A detailed description of the atmospheric correction method can be found in Section 2.1 of Lee et al. (2017). To intercalibrate AMSR-E and AMSR2 TBs, AMSR2 TBs are converted into AMSR-E-equivalent TBs based on the inter-calibration coefficients given in Table 2 (JAXA, 2015). Data close to coastlines within a distance of 100 km are discarded to prevent land contamination effects due to the large footprint of PMW observation, which can cause systematic errors in retrievals (Cavalieri et al., 1999;

Schluessel and Lurhardt, 1991). The retrievals are done only over the area where the sea ice concentration (SIC) is greater than 98% to avoid open water contamination.

Table 2. Intercalibration coefficients between AMSR-E and AMSR2. Conversion equation is $TB_{\text{AMSR-E}} = (1 - s)\ TB_{\text{AMSR2}} - i$.

Frequency/Polarization	**Slope (*s*)**	**Intercept (*i*)**
6.925 GHz/Vertical	-0.01390	3.67421
6.925 GHz/Horizontal	-0.00940	3.03663
10.65 GHz/Vertical	-0.01289	6.34775
10.65 GHz/Horizontal	-0.00221	3.79624
18.7 GHz/Vertical	-0.04524	12.57562
18.7 GHz/Horizontal	-0.00858	1.89574
36.5 GHz/Vertical	-0.01019	5.49799
36.5 GHz/Horizontal	-0.00985	4.19181

3.2.2. Snow surface temperature

To obtain the *TR*, time-averaged T_{as} is required. Recent T_{as} data for the 2020 period is obtained from the "Arctic Ocean – Sea and Ice Surface Temperature" dataset distributed by Copernicus Marine Environment Monitoring Service (CMEMS; https://marine.copernicus.eu). The T_{as} product was derived from Advanced Very High Resolution Radiometer (AVHRR) TBs at three channels (3.74, 10.8, and 12.0 μm) using the split-window algorithm (Dybkjær et al., 2014). For the 2003-2019 period, the data are obtained by personal communication with Dr. Gorm Dybkjær. Because those data are derived from AVHRR TBs using the same algorithm as the CMEMS T_{as} data, those two datasets are assumed a consistent T_{as} record for the 2003-2020 period. Daily T_{as} data in a 0.05° grid format is re-gridded to the 25 km grid. Finally, monthly fields of T_{as} are obtained by averaging daily fields under the condition of daily SIC greater than 98%.

3.2.3. Total freeboard

ICESat and ICESat-2 total freeboard (i.e., distance from a local sea surface to snow surface; depicted in Figure 1) measurements are used as a training dataset for obtaining the relationship between the SOD and total freeboard. Both are satellite lidar altimeters that measure the total freeboard by analyzing signals reflected at snow or sea surface. Both data are available at the NSIDC website (https://nsidc.org).

For ICESat data, along-track total freeboard measurements included in the "Arctic Sea Ice Freeboard and Thickness, Version 1" dataset (Yi and Zwally, 2009) are used. To match ICESat total freeboard with daily AMSR measurements, the track data are collocated in the 25 km grid format, producing daily total freeboard fields. The daily total freeboard fields are constructed for all available ICESat data February-March months during 2003-2008. For ICESat-2 data, daily gridded sea ice freeboards on 25 km gird included in the "ATLAS/ICESat-2 L3B Daily and Monthly Gridded Sea Ice Freeboard, Version 1" dataset (Petty et al., 2020; ATL20) are used. It is reported that ATL20 contains erroneous freeboards higher than few kilometers, therefore, freeboards higher than 1000 m are removed. All available ICESat-2 data are used over JFM months during 2019-2020.

Information on the satellite data used in this study is summarized in Table 3.

Table 3. Summarized information of satellite data

Variable	Sensor	Data period	Spatial resolution	Temporal resolution	Purpose	Data provider
T_{si}					*TR* calculation	
SOD	AMSR	2003-2020	25 km PSN format	Daily	F_t calculation	JAXA
Ice type					Analysis	
T_{as}	AVHRR	2003-2020	0.05°×0.05° grid	Daily	*TR* calculation	CMEMS
F_t	ICESat	2003-2008	170 m along track	Occasional	Training	NSIDC
	ICESat-2	2019-2020	25 km PSN format	Daily	Training	NSIDC

PSN: Polar Stereographic grid for Northern hemisphere (https://nsidc.org/data/polar-stereo/tools_geo_pixel.html)

3.3. Auxiliary data

Daily gridded 25 km SIC data included in the “NOAA/NSIDC Climate Data Record of Passive Microwave Sea Ice Concentration, Version 3” dataset are used (Meier et al., 2017a) to apply SIC criteria during the data processing. This SIC data set is a combination of ice concentration estimates from the NASA Team algorithm (Cavalieri et al., 1984) and the NASA Bootstrap algorithm (Comiso, 1986). The data are in the 25 km format and available from 9 July 1987 to 31 December 2019. In the case of the year 2020, a near-real-time version of the CDR data is used (Meier et al., 2017b).

Total freeboard and snow depth measurements are needed for snow depth retrieval and validation. Those measurements are available from NASA’s OIB mission. OIB is an aircraft mission and measures total freeboard and snow depth over the Arctic ocean using DMS, ATM, and snow radar (Kurtz et al., 2013). More information on the OIB mission can be found in Section 2.2.1. All available March OIB data during the 2009–2018 period are utilized in this study. The 2009-2013 period data are obtained from the “ICEBridge L4 Sea Ice Freeboard, Snow Depth, and Thickness, Version 1” dataset (Kurtz et al., 2015), and 2014-2018 period data are obtained from the OIB Quick Look dataset (available at https://doi.org/10.5067/GRIXZ91DE0L9). The OIB data are collocated on the 25

km grids by averaging the nearest OIB observations to grid point to produce daily gridded data.

Table 4. Summarized information of auxiliary data

Product	Sensor	Data period	Spatial resolution	Temporal resolution	Purpose	Data provider
SIC	SSMI SSMI/S	2003-2020	25 km PSN format	Daily	Sea ice mask	NSIDC
h_s	Snow radar	2009-2018	40 m along track	Occasional	Validation	NSIDC
F_t	ATM	2009-2018	40 m along track	Occasional	Validation	NSIDC

PSN: Polar Stereographic grid for Northern hemisphere (https://nsidc.org/data/polar-stereo/tools_geo_pixel.html)

4. Methods

4.1. Algorithm development

4.1.1. New method using thickness ratio (*TR*)

As described in the introduction, a relationship between snow depth and ice thickness can be used for retrieving snow depth from sea ice freeboard. To do so, this study defines the thickness ratio *TR* which is a ratio between h_s and H_i (i.e., $TR = h_s/H_i$). In this section, how snow depth and ice thickness can be obtained from the buoyancy equation with *TR* specified.

The buoyancy equation describes the Archimedes principle, which is a balance between the snow and ice loading and the buoyant force proportional to the submerged volume to the seawater. The equation is as follow:

$$\rho_i H_i + \rho_s h_s = \rho_w (H_i - F_i) \tag{1}$$

Here, F_i is the ice freeboard depicted in Figure 1. ρ_w, ρ_i, and ρ_s denote the bulk densities of water, ice, and snow layer, respectively. In Equation (1), there are three unknowns for given densities; Those are h_s, H_i and F_i. Unknown F_i can be obtained from satellite altimeter observations, but direct measurement of the F_i is not available yet.

Generally, there are two types of satellite altimeters providing indirect measurements of F_i: (1) Lidar altimeters such as NASA's ICESat (Zwally et al., 2002) and ICESat-2 (Markus et al., 2017) missions measure the total freeboard (F_t): the height from the sea surface in cracks and leads to the snow surface. (2) Radar altimeters such as ESA's CryoSat-2 (Wingham et al., 2006) measure the radar freeboard (F_r): difference in the radar ranging between the sea surface and the radar scattering horizon. The two different freeboards are indicated in Figure 1. In the case of total freeboard, ice freeboard can be obtained by simply subtracting snow depth from the total freeboard as the following equation:

$$F_i = F_t - h_s \tag{2}$$

On the other hand, obtaining ice freeboard from the radar freeboard is relatively complicated. Ice freeboard is obtained from radar freeboard by applying two correction terms regarding the change of the wave propagation speed in the snow layer (F_c) and the displacement of the scattering horizon from the ice surface (F_p) (Kwok and Cunningham, 2015).

$$F_i = F_r + (F_c - F_p) \tag{3}$$

The correction terms are expressed by the following equations (Armitage and Ridout, 2015; Kwok and Markus, 2018).

$$F_c = (\eta_s - 1) f h_s \tag{4}$$

$$F_p = (1 - f) h_s \tag{5}$$

Here, η_s denotes the refractive index of the snow layer and f denotes the radar penetration factor (Armitage and Ridout, 2015), which is the depth of the radar scattering horizon relative to the snow depth (e.g., f = 1 if the radar scattering horizon is at snow–ice interface and f = 0 if the radar scattering horizon is at air-snow interface). A combination of Equations (3)–(5) yields the following relationship.

$$F_i = F_r + (f \eta_s - 1) h_s \tag{6}$$

Using Equations (2) and (6), Equation (1) can be rewritten as follows:

$$\rho_w F_t = (\rho_w - \rho_i) H_i + (\rho_w - \rho_s) h_s \tag{7}$$

$$\rho_w F_r = (\rho_w - \rho_i) H_i - \{(f \eta_s - 1) \rho_w + \rho_s\} h_s \tag{8}$$

Finally, substituting h_s with $TR \times H_i$ by definition yields an equation for ice thickness in terms of TR and F_t (or F_r).

$$H_i = \frac{\rho_w}{\rho_w - \rho_i + (\rho_w - \rho_s) TR} F_t \tag{9}$$

$$H_i = \frac{\rho_w}{\rho_w - \rho_i - \{(f\eta_s - 1)\rho_w + \rho_s\}TR} F_r \quad (10)$$

At the same time, the corresponding h_s is obtained by multiplying the obtained H_i and TR. From Equations (9) and (10) it is evident that the snow depth and ice thickness can be simultaneously estimated from the freeboard measurements and TR, once ρ and f are known.

Currently, there are some parametrizations available for snow and ice densities, which can be chosen by users upon their purpose. On the other hand, the radar penetration factor f remains widely uncertain for various retracker algorithms and various ice types and conditions (Nandan et al., 2017; Willatt et al., 2011; Tonboe et al., 2010). Therefore, this study uses total freeboard with Equation (9) rather than radar freeboard for snow depth estimation.

4.1.2. Theoretical background of *TR*

To retrieve the snow depth in the Arctic basin-scale, the way to resolve *TR* in such scale is only possible through satellite observations. Since the vertical thermal structure of a snow-ice system can be resolved from satellite observations, we now explore whether *TR* can be described in terms of the vertical thermal structure. To do so, we consider a physical property relating the thickness to temperature, i.e., the conductive heat flux, which is a derivative of temperature to depth multiplied by thermal conductivity.

The conductive heat flux across the snow-ice interface is assumed to be continuous (Maykut and Untersteiner, 1971) and expressed as in the following equation:

$$k_{snow} \left. \frac{\partial T_{snow}}{\partial z} \right|_{z=0} = k_{ice} \left. \frac{\partial T_{ice}}{\partial z} \right|_{z=0} \tag{11}$$

In Equation (11), the subscripts *snow* and *ice* denote their respective layers, and T, k, and z denote temperature, bulk thermal conductivity, and depth, respectively. Here, the snow-ice interface locates at $z = 0$. This heat flux continuity assumption has been widely accepted for sea ice studies regarding thermodynamic modeling, satellite application, and in situ measurements for snow and ice conductivities (Maykut and Untersteiner, 1971; Maaß et al., 2013; Perovich et al.,

1997). Besides, temperature discontinuity at the snow-ice interface must be observed if Equation (11) is not valid. However, such discontinuity has not been observed in buoy data used in this study, thus it is plausible to use this assumption.

Equation (11) can be rewritten as the following equation, assuming a piecewise linear temperature profile within the snow and ice layers.

$$k_{snow}\frac{T_{as}-T_{si}}{h_s}=k_{ice}\frac{T_{si}-T_{iw}}{H_i} \tag{12}$$

Subscripts *as*, *si*, and *iw* denote the air-snow, snow-ice, and ice-water interface, respectively, as depicted in Figure 1. For the piecewise linear temperature profile assumption, it is necessary to average the temperature profile over weekly to monthly timescale. Shi et al. (2020) analyzed the buoy-measured sea ice temperature profiles with various averaging periods from 1 to 30 days to figure out which averaging timescale can satisfy the assumption. It was found that averaging periods longer than 7 days are suitable to approximate the linear temperature profile of sea ice.

Then, the rearrangement of Equation (12) yields the relationship between *TR* and the vertical thermal structure as follow:

$$TR=\frac{h_s}{H_i}=\frac{k_{snow}}{k_{ice}}\frac{\Delta T_{snow}}{\Delta T_{ice}} \tag{13}$$

Here, ΔT denotes the temperature difference between the top and bottom of the snow or ice layer (i.e., $\Delta T_{snow} = T_{as} - T_{si}$ and $\Delta T_{ice} = T_{si} - T_{iw}$). One may concern that Equation (13) is a highly simplified equation while the Arctic snow-ice system has a complex multi-layer vertical structure. However, an equivalent equation to Equation (13) can be derived by taking a different approach of physical insight. The ΔT of a certain layer should be proportional to the thickness of the corresponding layer considering an insulating effect. Therefore, TR should be proportional to ΔT_{snow} and inverse proportional to ΔT_{ice}. This is equivalent to the form of Equation (13).

4.1.3. Strategy for obtaining *TR*

In this section, a strategy to find an empirical equation that can predict *TR* from the T_{as}, T_{si}, and T_{iw} based on the form of Equation (13) is described. In order to calculate *TR* from interface temperatures, the thermal conductivity ratio (k_{snow}/k_{ice}) should be known. There can be two approaches to obtain the conductivity ratio: (1) to use parametrization on thermal conductivity of snow and sea ice or (2) to use in-situ data to obtain the ratio statistically.

The first approach requires us to review the factors determining k_{ice} and k_{snow}. According to Maykut and Untersteiner (1971), k_{ice} is a function of salinity and temperature.

$$k_{ice} = 2.03 + 0.117\frac{S_{ice}}{T_{ice}} \quad (\mathrm{W\,K^{-1}\,m^{-1}}) \tag{14}$$

Here, S_{ice} and T_{ice} are the salinity (in part per thousand; ppt) and temperature (in Celsius) of sea ice, respectively. S_{ice} can be estimated according to the following empirical relationship between sea ice thickness and mean salinity from Cox and Weeks (1974):

$$S_{ice} = \begin{cases} 14.24 - 19.39H_i, & H_i \le 0.4\,\mathrm{m} \\ 7.88 - 1.59H_i, & H_i > 0.4\,\mathrm{m} \end{cases} (\mathrm{ppt}) \tag{15}$$

We can use Equations (14) and (15) to calculate k_{ice} without additional unknowns. However, the calculation of k_{snow} is much more complex. k_{snow} is

determined by snow density, temperature, and crystal structure (Sturm et al., 1997). Snow is a mixture of ice particles and air, and air has lower thermal conductivity than ice. Thus, snow with a relatively lower density including a greater portion of air should have relatively lower thermal conductivity. Besides, the thermal conductivity of ice particles depends on the temperature and the path of heat transfer depending on the crystal structure (e.g., how the ice particles are connected). The heat transfer occurs not only by conduction but also by water vapor latent heat transportation and convection through the pore spaces (Sturm et al, 2002), which are hard to quantify explicitly.

In short, it is impossible to calculate k_{snow} explicitly from satellite observation. Therefore, instead of explicit calculation of thermal conductivities, this study takes the second approach which empirically determines the *TR*-temperature equation using *TR* and $\Delta T_{snow}/\Delta T_{ice}$ obtained from the in-situ buoy temperature profile measurements.

4.1.4. Buoy data preprocessing

To determine the *TR*-temperature equation from in-situ measurements, values of h_s, H_i, T_{as}, T_{si}, and T_{iw} (as depicted in Figure 1) are required. For obtaining required variables, the interfaces should be determined from buoy-measured temperature profiles, which show a piecewise linear temperature profile as schematically depicted in Figure 1. The temperature profiles are measured by thermistor string where temperature sensors are installed at discrete levels. It means that the interfaces (air–snow, snow–ice, and ice–water) can be located in-between measurement levels. Moreover, although the instrument initially sets the zero-depth reference position to be approximately at the snow–ice interface, the reference position can deviate from the initial position due to the ice deformation, the metamorphosis of snow into snow-ice. Therefore, an interface searching algorithm is developed to search three interfaces (y_{as}, y_{si}, y_{iw}) and their respective temperatures (T_{as}, T_{si}, T_{iw}).

The interface searching algorithm iterates the following three processes to find the location and temperature at each interface: (1) dividing temperature profile into four layers using the most recently available locations of the three interfaces, (2) finding a linear regression line of the temperature profile at each layer, (3) updating the location and temperature of each interface by finding an intersection between two adjacent regression lines. The algorithm fails to search

interfaces if the temperature profile of the ice layer is far from linear, or the thickness of a certain layer is too thin (i.e., having less than two data points which are the minimal set to determine a regression line) or the difference between the maximum and minimum temperature within water layer exceeds 0.5 K. The final outputs are T_{as}, T_{si}, T_{iw}, H_i ($= y_{as} - y_{si}$), and h_s ($= y_{si} - y_{iw}$). Detailed procedures for determining the interface are provided in Figure 6, as a flow chart. To secure the required vertical thermal states (e.g., linear temperature profile), monthly averaged temperature profiles are used as input to the interface searching algorithm.

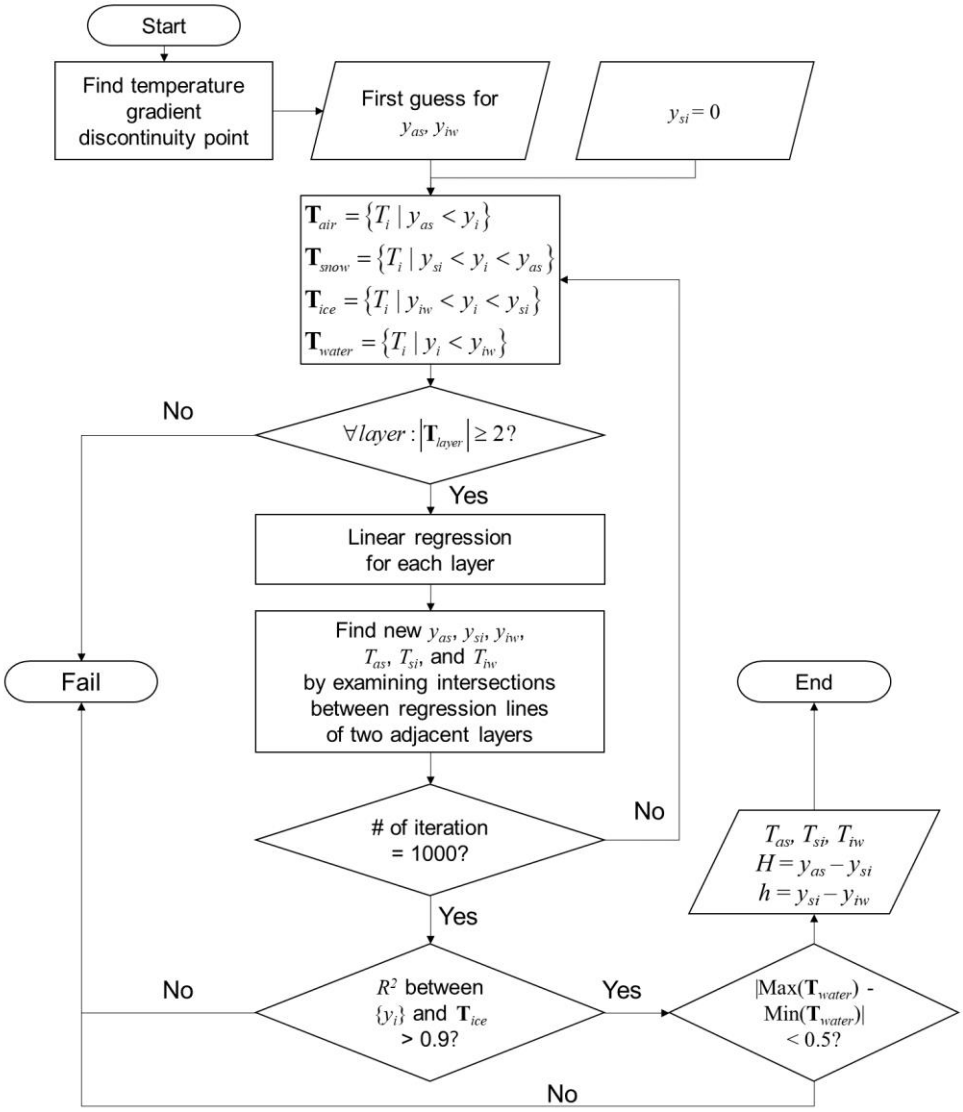

Figure 6. The flow chart of the interface searching algorithm. y_i and T_i denote the position and temperature of a data point in the temperature profile. y_{as}, y_{si}, and y_{iw} denote the position of the interfaces, and $\mathbf{T}_{layer}$ denotes a set of temperature data points.

4.1.5. Snow depth retrieval procedure

The snow depth retrieval procedure consists of two steps. First, *TR* is calculated from satellite-derived T_{as} and T_{si} with constant T_{iw} using the *TR*-temperature equation. To do so, T_{iw} is assumed to be a constant as a freezing temperature of seawater and its value is chosen as the average value of T_{iw} in buoy data. Second, h_s is calculated from the obtained *TR* and F_t measurements using Equation (9) with prescribed densities.

For calculating *TR*, time-averaged fields of T_{as} and T_{si} are required because the *TR*-temperature equation is based on the analysis of monthly averaged buoy data. However, the literal meaning of monthly average is not a necessary condition for the application. Therefore, moving average with a 31-day time window is done to produce a daily time-averaged temperature field. In this case, the date at the center of the time window represents the observation time of the averaged data. Daily temperature fields applied with 98% SIC mask (SIC > 98%) are used for the moving average calculation. Finally, *TR* is calculated but rejected if T_{as} is warmer than T_{si}.

Now h_s can be estimated from Equation (9) using *TR* and F_t with prescribed density values. The densities are prescribed as those used for Operation ICEBridge (OIB) data processing (Kurtz et al., 2013) because we intend to compare outputs

against OIB data: ρ_s, ρ_i, and ρ_w are 320 kg m^{-3}, 915 kg m^{-3}, and 1024 kg m^{-3}, respectively. Currently, there is an issue about sea ice density in the field of satellite sea ice thickness retrieval. While some studies (e.g., Petty et al., 2020; Kurtz et al., 2013; Kurtz and Harbeck, 2017) have used a uniform sea ice density assumption across the Arctic basin as 915 kg/m^3 for ice density for sea ice thickness estimation from satellite and airborne altimetry, other studies discriminate sea ice density according to sea ice type as suggested by Alexandrov et al. (2010). They suggested values of 882 kg/m^3 for MYI density and 917 kg/m^3 for FYI density. Here, short discussion on the two-density assumption suggested by Alexandrov et al. (2010) is made.

To estimate the density of FYI, Alexandrov et al. (2010) used Sever expedition data which provides in situ-measured snow density, snow depth, ice freeboard, and sea ice thickness, considering that SEVER expedition was done over FYI. However, their conjecture on sea ice type is questionable because Sever data does not provide any ice type information, and approximately 30% of Sever measurements were found to be done over MYI when the geolocations of each measurement are matched with the satellite-derived NSIDC ice age data (Tschudi et al., 2019a) for 1984-1988 period when both datasets are available. This implies that the density of MYI can be close to the density of FYI.

In the case of MYI density, weighted averaged density of freeboard layer and

draft layer (i.e., submerged part of sea ice) was used based on the difference in compositional characteristic between freeboard and ice draft layers. While the density of the freeboard layer depends largely upon ice type, the density of the ice draft layer is nearly uniform approximately 920 kg m^{-3} regardless of ice type (Timco and Frederking, 1996). During summer, brine rejection occurs resulting in air pockets replacing brine pockets in the freeboard layer. Therefore, the freeboard layer of MYI generally has a lower density value than that of FYI because of the relatively larger amount of air pockets in the freeboard layer of MYI. However, considering that the magnitude of such difference is around 20 kg m^{-3} and freeboard occupies only 10% of ice thickness, it seems that there would be no significant differences in bulk sea ice density between FYI and MYI. As Arctic basin-scale measurements for sea ice density are lacking, further study should be needed to evaluate which sea ice density is plausible. At this point, it is reasonable to select 915 kg m^{-3} for sea ice density.

4.2. Sea ice parameters from satellite PMW measurements

4.2.1. Simplified radiative transfer model

In the case of specular and homogeneous sea ice without snow cover, upwelling *p*-polarized radiance T_p at the ice surface can be formulated as multiplication of *p*-polarized Fresnel surface emissivity $\varepsilon_{s,p}$ (subscript *s* denotes specular) and effective emission temperature T_E.

$$TB_p = \epsilon_{s,p} T_E \tag{16}$$

Here, $\varepsilon_{s,p}$ is a function of adjusted real refractive index N_r. This simple formulation is valid for lower microwave frequencies such as the 6.925 GHz channel. However, surface roughness and scattering should be considered for higher frequency. To include those effects, Lee et al. (2018) introduced a simplified three-layer radiative transfer model for a snow-ice system that can be used for microwave frequencies below 37 GHz. It consists of a snow layer at the top, a surface scattering ice layer in the middle, and a congealed ice layer at the bottom as illustrated in Figure 7.

In the simplified model, upwelling polarized radiance is emitted from a hypothetical rough emission surface located in the middle and/or bottom layers and attenuated by snow particles and air pockets in the freeboard above the

emission layer. Then TB_p emanating from the top of the snow surface can be written as the following equation.

$$TB_p = \epsilon_{r,p} e^{-\tau_{sca}} T_E \tag{17}$$

In Equation (17), $\varepsilon_{r,p}$ is a rough surface emissivity described by two-dimensional isotropic rough surface emissivity model (Lee et al., 2018; see Sect. 2.1 and Appendix A of their paper), which is a function of N_r and root-mean-square slope of the surface σ (referred to as roughness index), and τ_{sca} denotes SOD. For the practical purpose, apparent emissivity ε_p is defined as the ratio between T_E and TB_p.

$$\epsilon_p = TB_p / T_E \tag{18}$$

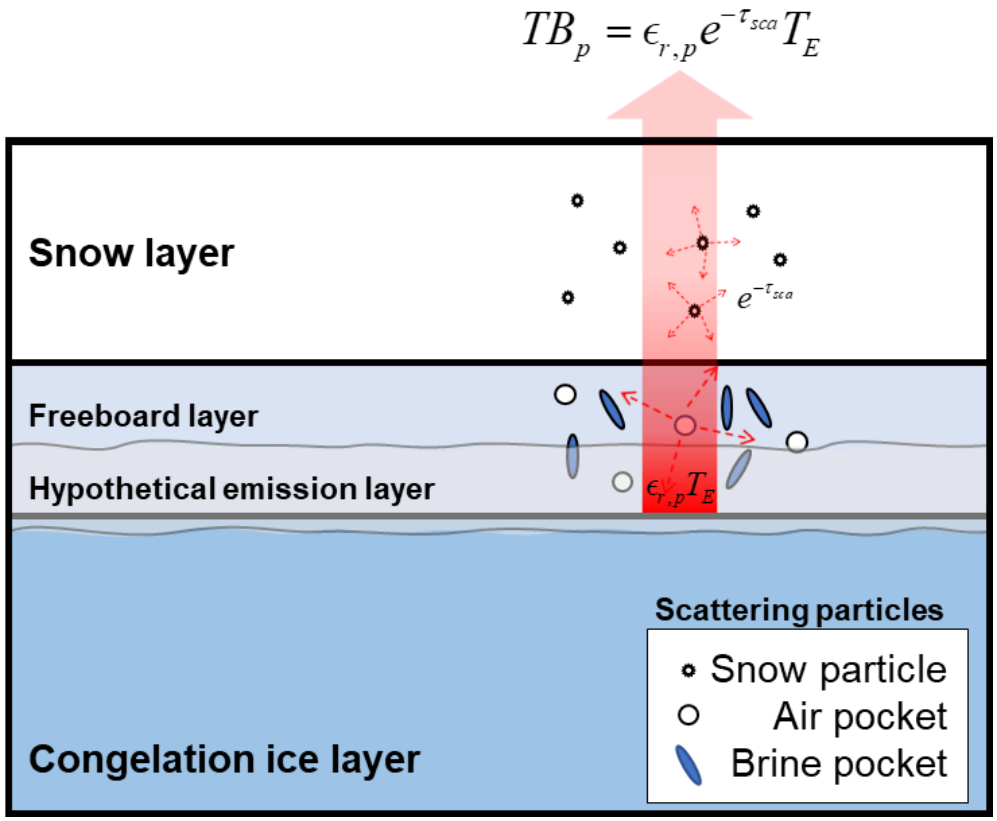

Figure 7. Schematic diagram of simplified three-layer radiative transfer model.

4.2.2. Snow-ice scattering optical depth

Combining Equations (17) and (18), the following relationship is obtained.

$$\epsilon_p = \epsilon_{r,p}(N_r, \sigma)e^{-\tau_{sca}} \tag{19}$$

To solve Equation (19) for τ_{sca} at a certain frequency, values of N_r, ε_p, and σ should be known. This can be done based on the optical characteristics of sea ice in the microwave region. First, N_r over sea ice has a nearly invariant behavior over the microwave frequencies of interest (Vant et al., 1978; Ulaby et al., 1986; Warren and Brandt, 2008). Second, T_E at frequencies between 6.925 GHz and 36.5 GHz are similar (Lee and Sohn, 2017).

Therefore, we can use N_r and T_E at one frequency for another frequency. For simultaneous retrieval of N_r and T_E, the algorithm developed by Lee and Sohn (2015) using polarized TB measurements from AMSR at 6.925 GHz is used. As T_E is obtained, ε_p can be calculated for each frequency from Equation (18) after removing the atmospheric contribution from observed TB.

Once N_r is prescribed in, σ and τ_{sca} can be solved since there are observations from two independent polarizations (i.e., vertical and horizontal polarization). For computationally efficient calculation, method introduced by Lee et al. (2021) using polarization ratio (PR) defined as $PR = (TB_V - TB_H)/(TB_V+TB_H)$ is used.

Because PR decreases with σ for given N_r as shown in Figure 8a, σ can be solved by minimizing the difference between simulated and observed PR. The processes for retrieving σ are summarized in Figure 8b. Finally, τ_{sca} can be solved from (19) as N_r, ε_p, and σ are obtained.

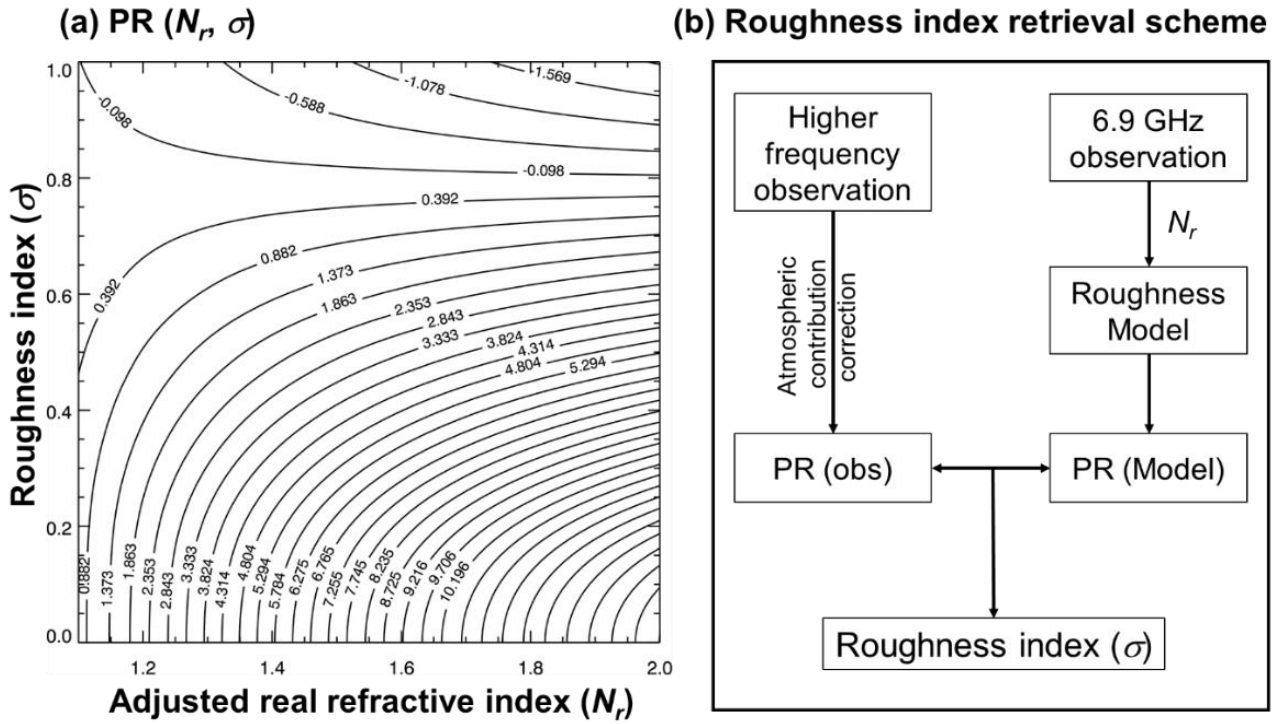

Figure 8. (a) Contours of polarization ratio (PR) × 100 with respect to the adjusted real refractive index (N_r) and roughness index (σ) and (b) roughness index (σ) retrieval scheme.

4.2.3. Sea ice type

There are two distinct groups of Arctic sea ice during boreal winter. Those are FYI and MYI which are newly formed ice and the ice survived melting season, respectively. As the physical properties of FYI and MYI are significantly different it is worth analyzing results for each ice type.

The difference in radiative properties between FYI and MYI enables us to discriminate two ice types from satellite PMW measurements. Sea ice experiences a brine rejection process during the summer melting period, as known as brine drainage that reduces the salinity of the ice above the waterline (i.e., freeboard layer). The most accepted mechanism for the brine drainage to the researchers is flushing (Untersteiner, 1968). In that mechanism, fresh water produced by surface melting flushes out the brine inclusions downward through permeable sea ice that allows meltwater to penetrate. However, such flushing is limited to the level near the waterline because the height difference between the level of meltwater and waterline is needed for a downward gravitational force that is a source of flushing. As a result of brine drainage, MYI has lower salinity and more air pockets than FYI in the freeboard layer. This physical property of MYI is related to a deeper emitting layer with more scattering, and thus reduces the apparent emissivity of MYI.

Lee et al. (2017) retrieved apparent emissivities defined in Equation (18) from AMSR-E measurements and analyzed their spectral signature in order to separate sea ice types using PMW measurements. They found that apparent emissivity of MYI generally decreases with frequency while the apparent emissivity of FYI shows less spectral difference (Figure 9). Based on this finding, Lee et al. (2017) suggested that the difference of vertically polarized apparent emissivity ε_V between 10.65 GHz and 18.7 GHz can separate FYI and MYI. Such index referred to as EVD is defined as the following equation.

$$\mathrm{EVD} = \epsilon_V(10.65\,\mathrm{GHz}) - \epsilon_V(18.7\,\mathrm{GHz}) \tag{20}$$

In general, the EVD value is positive for MYI and slightly negative for FYI as observed in Figure 9. The geographical distribution of EVD is shown in Figure 10a and the boundary between FYI and MYI is clearly observed.

There is another satellite product related to sea ice type available at NSIDC. The product named “EASE-Grid Sea Ice Age, Version 4” (Tschudi et al., 2019a) provides weekly estimates of sea ice age over the Arctic Ocean derived from remotely sensed sea ice motion and SIC in 12.5 km x 12.5 km grid format. As the principle of sea ice tracking is simple and robust, it is thought that the quality of the sea ice age product for separating FYI and MYI is most reliable among other satellite products. Here, EVD is compared with the NSIDC ice age product shown

in Figure 10b. They seem consistent with each other in terms of the geographical distributions of MYI (i.e., positive EVD and ice age older than 1). Based on the comparison, it is expected that sea ice separation results will not significantly differ whatever data is used. However, EVD-based sea ice type can provide daily data and the grid is perfectly matched with other data used in this study. Therefore, this study utilizes daily sea ice type data based on EVD.

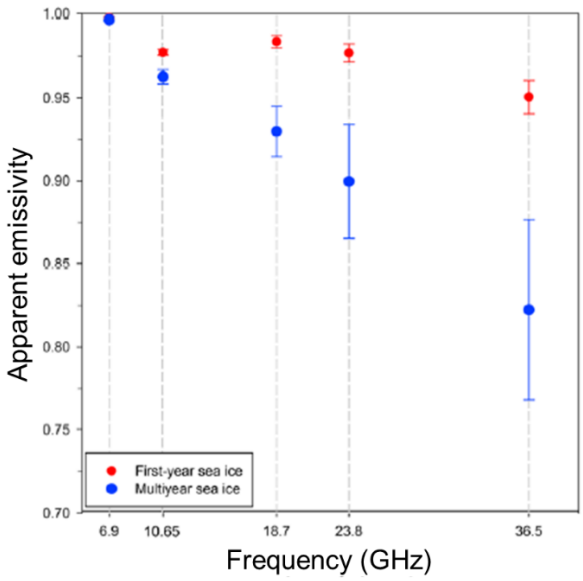

Figure 9. Nine-year (2003–2011) January mean vertically polarized apparent emissivities averaged over first-year ice (red dots) and multiyear ice (blue dots). The error bar represents one standard deviation of the data (Figure from Lee et al., 2017).

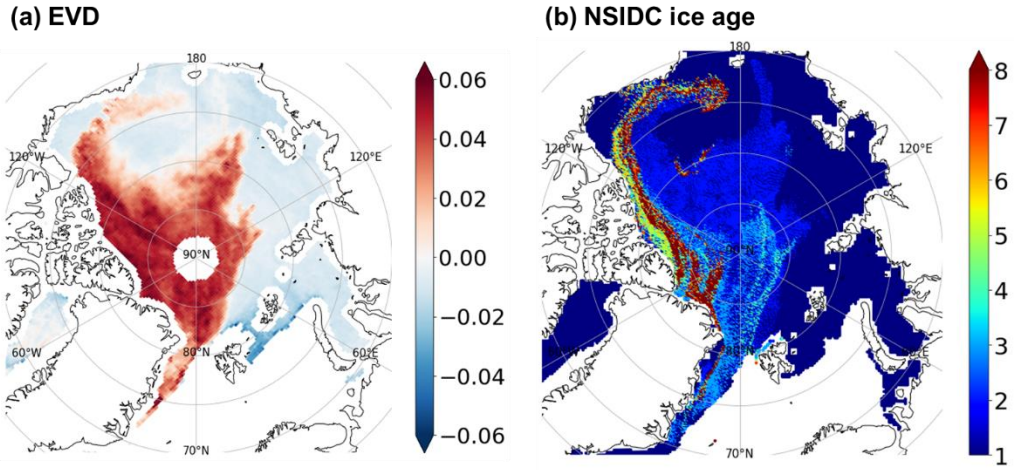

Figure 10. Geographical distributions of (a) EVD for 1 January 2010, and (b) NSIDC ice age product for the first week of January 2010.

5. Results

5.1. Snow depth retrieval algorithm

5.1.1. *TR*-temperature equation

In order to find the *TR*-temperature equation in the form of Equation (13) using in-situ data, first, T_{as}, T_{si}, T_{iw}, H_i, and h_s were obtained from buoy measured temperature profiles. To do so, the interface algorithm introduced in Section 4.1.4 was applied to monthly averaged temperature profiles. An example of the interface searching result for AWI buoy measurement in March 2014 is shown in Figure 11. The algorithm worked adequately for the rest of the AWI buoy measurements in Table 1. Since the required variables were obtained from the buoy temperature profiles using the interface searching algorithm, the calculations of $\Delta T_{snow}/\Delta T_{ice}$ and *TR* are straightforward.

Now, let us examine obtained variables to obtain the *TR*-temperature equation. In Figure 12, the scatter plot of $\Delta T_{snow}/\Delta T_{ice}$ versus *TR* for JFM months is shown. It appears that *TR* has a linear relationship with $\Delta T_{snow}/\Delta T_{ice}$. Such pattern is found to be nearly invariant regardless of months, as different markers representing the month of observation appear through the entire range of $\Delta T_{snow}/\Delta T_{ice}$. Taking such a linear pattern of *TR* with respect to $\Delta T_{snow}/\Delta T_{ice}$ into account, the *TR*-temperature

equation was determined by doing linear regression using 42 data points. The found equation is as follow:

$$TR = 0.11 \times \frac{\Delta T_{snow}}{\Delta T_{ice}} + 0.04 \tag{21}$$

To evaluate the performance of the regression analysis, predicted *TR* values from Equation (21) are compared to the original *TR* values. The comparison revealed that the regression equation was fitted well based on a mean bias of zero, a root-mean-squared difference (RMSD) of 0.02, and a coefficient of determination (R^2) of 0.82. Therefore, we can estimate *TR* using Equation (21) if T_{as}, T_{si}, and T_{iw} are known.

For the Arctic basin-scale retrieval of *TR*, satellite-derived temperature data are available for T_{as} and T_{si}. T_{iw} is set to be a constant freezing temperature of seawater. Although the freezing temperature of seawater is often assumed to be -1.8 °C, the value of -1.87 °C is chosen based on the buoy observations used in this study. A sensitivity test indicated that the influence of a 0.07 °C difference in the freezing temperature on *TR* was negligible.

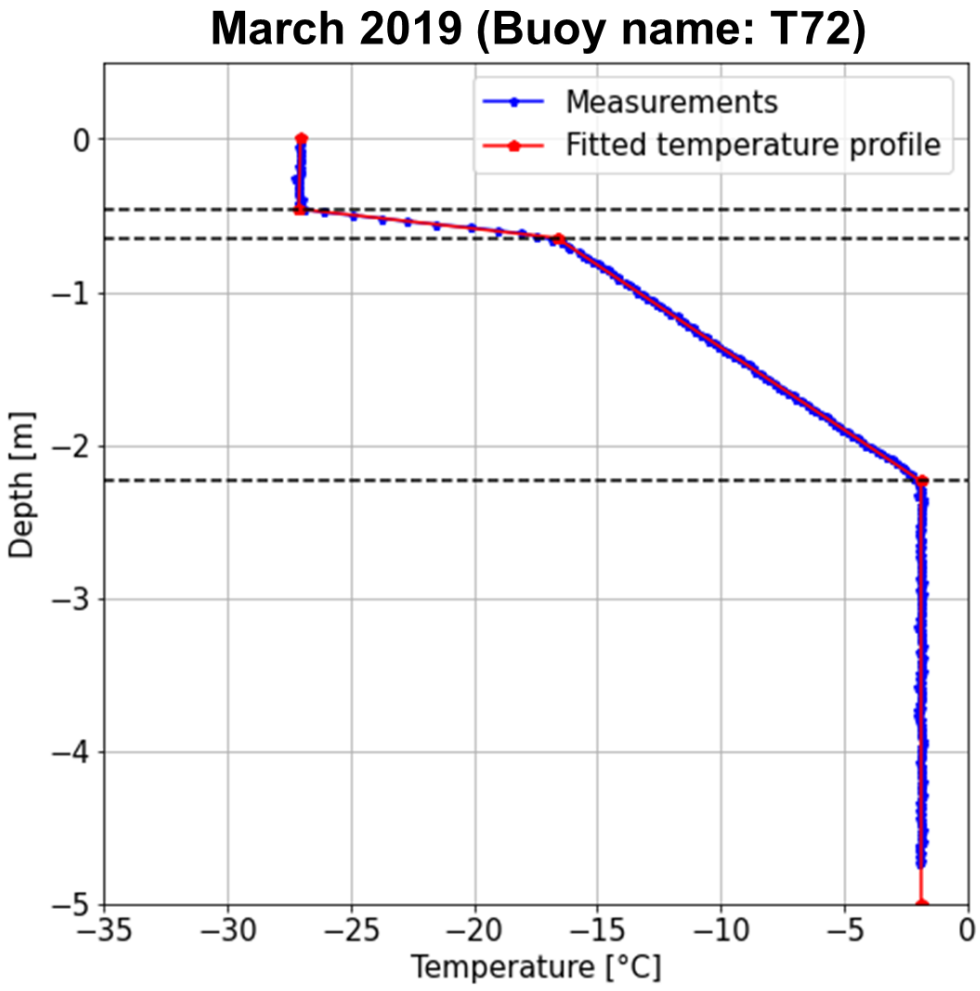

Figure 11. Example of interface searching results with monthly temperature profile from AWI 2019T72 buoy in March: Blue dots are buoy-measured temperature profiles and red lines are regression lines. Black dashed lines indicate the intersections between adjacent regression lines.

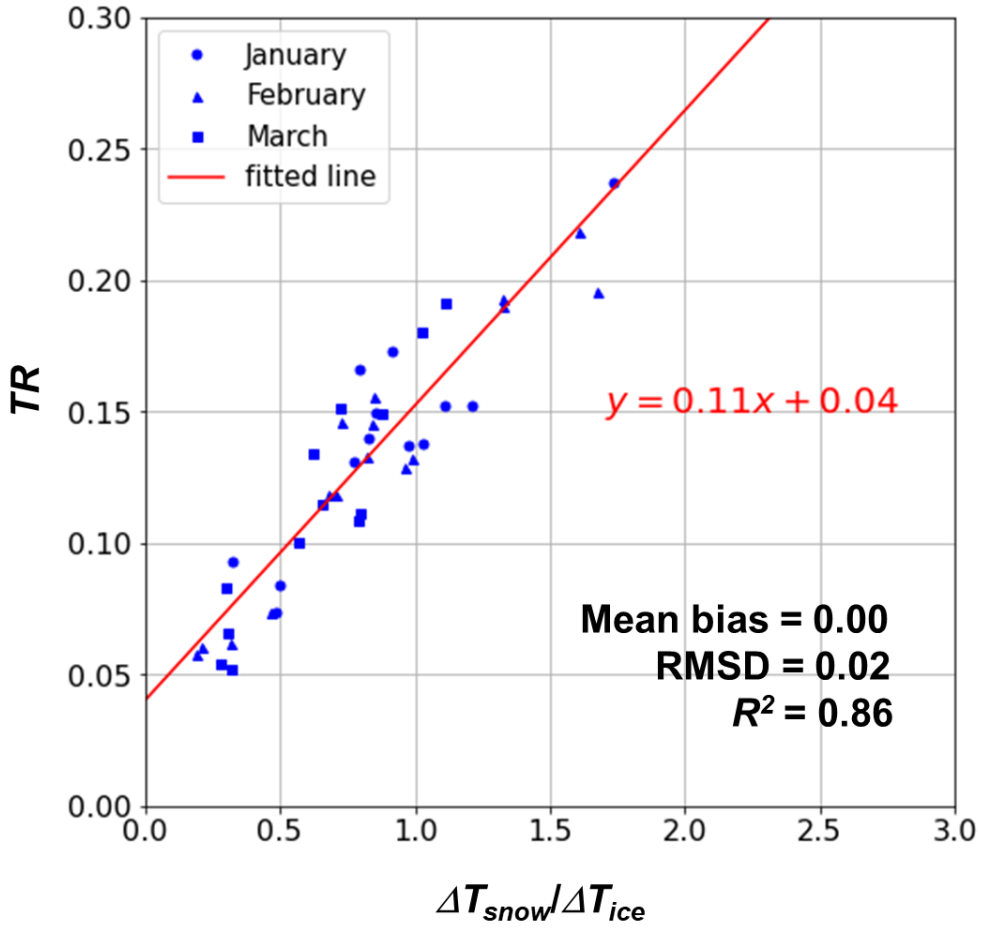

Figure 12. Scatter plots of the temperature difference ratio of the snow and ice layer ($\Delta T_{snow}/\Delta T_{ice}$) and the snow–ice thickness ratio (TR). The shape of the marker denotes the collected month of buoy data. The red solid line is the regression line defined in Equation (21). Error statistics are included in the figure.

5.1.2. Snow depth retrieval and validation

Snow depth can be retrieved from T_{as}, T_{si}, and F_t using Equation (21) and Equation (9). To test and evaluate the developed snow depth retrieval method, snow depth was retrieved using the OIB measured F_t with satellite-derived T_{as} and T_{si}, then the retrieved snow depth was compared with the independent OIB snow depth measurement. If the retrieved snow depth shows good agreement with the OIB snow depth, we can tell the developed retrieval algorithm works successfully.

To do so, snow depth was retrieved by using procedures described in Section 4.1.5. Daily *TR* was calculated from the 31-day running averaged T_{as} and T_{si} using Equation (21). Then, daily h_s was calculated with obtained *TR* and OIB measured F_t using Equation (9) with prescribed densities in Section 4.1.5. Geographical distributions of the retrieved snow depth and OIB snow depth are presented in Figure 13a and Figure 13b, respectively. Retrieved snow depths and the OIB measurements appear to be consistent with each other in terms of magnitudes and spatial patterns. To compare the results quantitatively, a 2-dimensional histogram comparing the retrieved h_s against OIB measurements was made from 816 matched data, along with error statistics (Figure 14). The comparison indicates that the retrieved snow depth is consistent with independent OIB snow depth measurements, with a correlation coefficient of 0.84, a near-zero bias of 0.19 cm, and an RMSD of 5.06 cm. It is also noted that the slope of the regression line

between the OIB and retrieved snow depth is approximately 1. Based on the validation result, the *TR*-temperature equation obtained from the buoy measurements is thought to be used for further Arctic basin-scale snow depth estimation.

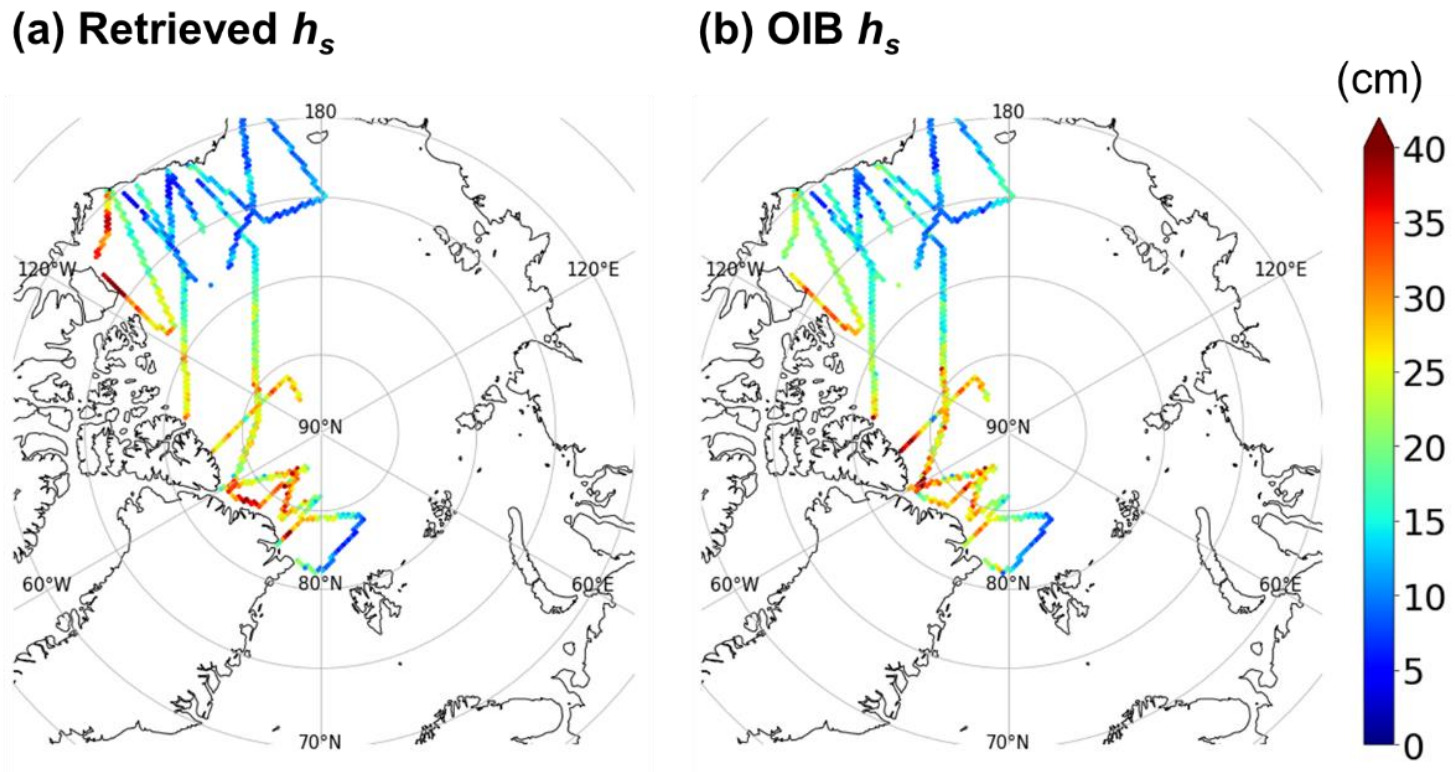

Figure 13. Geographical distributions of (a) snow depth retrieved from OIB total freeboard and satellite-derived *TR* and (b) snow depth from OIB snow radar for all matched data in March.

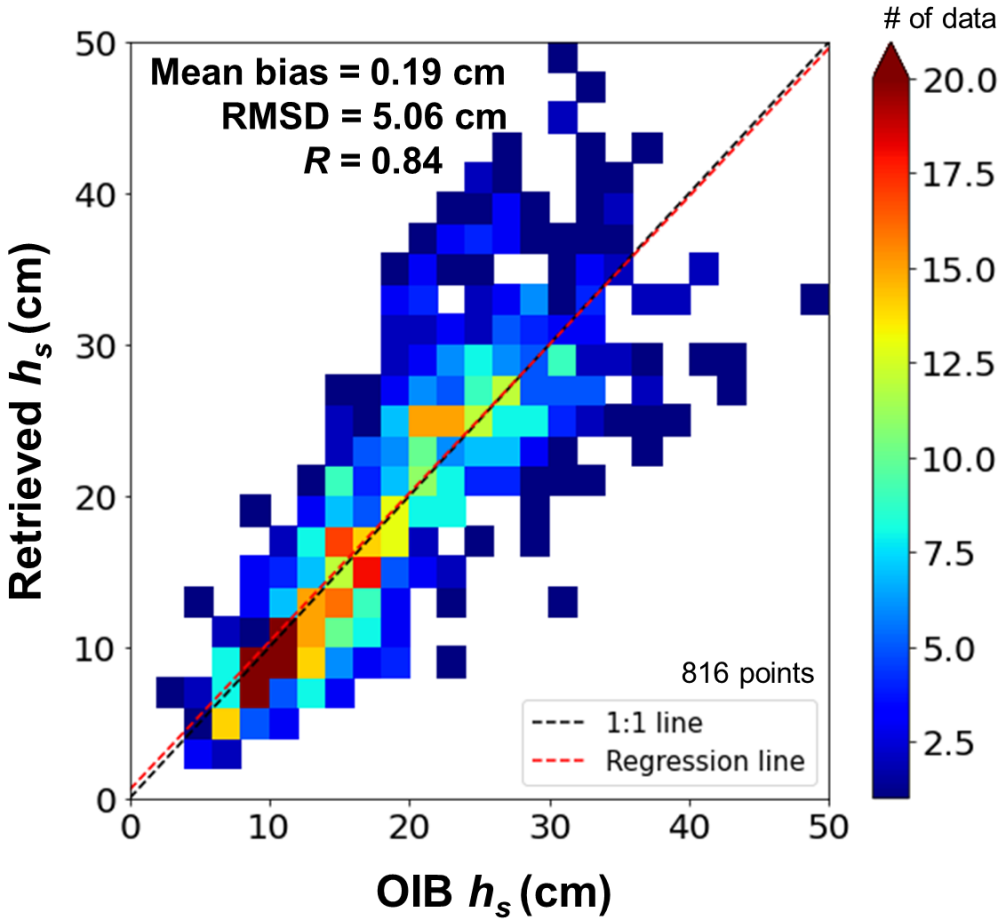

Figure 14. 2-dimensional histogram between OIB snow depth and the snow depth retrieved from OIB total freeboard and satellite-derived *TR* with error statistics and the regression line (red solid line).

5.2. Long-term snow depth record

5.2.1. PMW total freeboard

In the previous section, an algorithm using T_{as}, T_{si}, and F_t is introduced to retrieve the snow depth. To obtain the Arctic basin-scale snow depth record, continuous observations of the input variables with wide spatial coverage are necessary. While temperature data meet that condition, satellite F_t measurements have limitations on spatial coverage compared to the temperature data. As the total freeboard is measured by lidar altimeter, the relatively small footprint of lidar sensor and widespread cloud cover may limit the spatial coverage. This characteristic reduces the observation frequency at each location, causing the situation that the Arctic basin-scale F_t field should be obtained by a composite of daily observations for a period longer than a month. Therefore, obtaining F_t from PMW measurements is desirable.

Regarding this issue, Lee et al. (2021) demonstrated that the ice freeboard can be obtained from PMW measurements using the SOD of sea ice as a predictor. Their algorithm is based on the physical background that SOD reflects scattering effect due to air pockets in ice freeboard layer. However, total freeboard retrieval instead of ice freeboard would be more promising because SOD includes the scattering effect of snow particles as well. Moreover, CS2-derived ice freeboard

which was a target variable in their study has a great uncertainty due to the radar penetration factor and snow depth climatology used for the data production (Shi et al., 2020). Therefore, this study attempts to obtain F_t from SOD by conducting regression analysis to predict the F_t field with wider spatial coverage and more continuous temporal availability. To examine the possibility, geographical distributions of SOD at 36.5 GHz channel (hereafter, referred to as $SOD_{36.5}$) and total freeboard F_t in January 2020 are compared in Figure 15. Here, $SOD_{36.5}$ is obtained from AMSR measurements by the method described in Section 4.2.2. Spatial distributions of two variables look similar to each other. Especially, the boundary of the MYI region is clearly depicted in both distributions, rendering $SOD_{36.5}$ to be useful as a predictor for F_t.

To determine the empirical relationship between the scattering optical depth and the total freeboard, $SOD_{36.5}$ retrieved from daily AMSR-E and AMSR2 data were matched with F_t from daily ICESat and ICESat-2 data during 2003-2008 and 2019-2020 period. Total 338848 data points are matched as in the 2-dimensional histogram presented in Figure 16. A positive correlation between the $SOD_{36.5}$ and F_t can be observed from the 2-d histogram. As most of the data are at a region where the optical depth is less than 0.1, we conducted a binned analysis to obtain mean values and standard deviations which are used for further regression analysis. Means and standard deviations are calculated for every 0.01 bin of optical depth.

A significant linear relationship is found from the series of mean values.

To find a linear fit from mean and standard deviation values of each bin, the weighted least square is used in order to incorporate the variance of the F_t into the regression (i.e., regression focuses on the less uncertain data such as optimal estimation technique). Mean values were weighted with the inverse of standard deviation (i.e., the uncertainty of total freeboard). By doing so, a fitted line can be more focused on data with smaller uncertainty. Additionally, mean values calculated from less than 1000 data were not used for the regression as they would not represent the bin adequately. The obtained regression equation is as below:

$$F_t = 0.98 \times \mathrm{SOD}_{36.5} + 0.23 \tag{22}$$

Using Equation (22), daily F_t fields were retrieved for the AMSR period during winter (i.e., JFM of 2003-2020, except for 2012). Retrieved F_t was validated against OIB total freeboard measurements. Geographical distributions of retrieved F_t and OIB F_t are illustrated in Figure 17. Although their distributions are consistent, Equation (22) seems to underestimate the thick total freeboard in the area showing larger than 0.6 m. For quantitative comparison, 2d-histogram with statistics are made for 2792 matched data as in Figure 18. Compared to OIB F_t, retrieved F_t has a mean bias of -0.03 m, RMSD of 0.13 m, and a correlation coefficient of 0.67. Relatively large RMSD compared to the small mean bias may

be related to horizontal resolution difference between PMW and active laser sensors because the OIB F_t shows greater variance compared to the retrieved F_t. It is thought that Equation (22) can estimate F_t adequately in terms of mean bias.

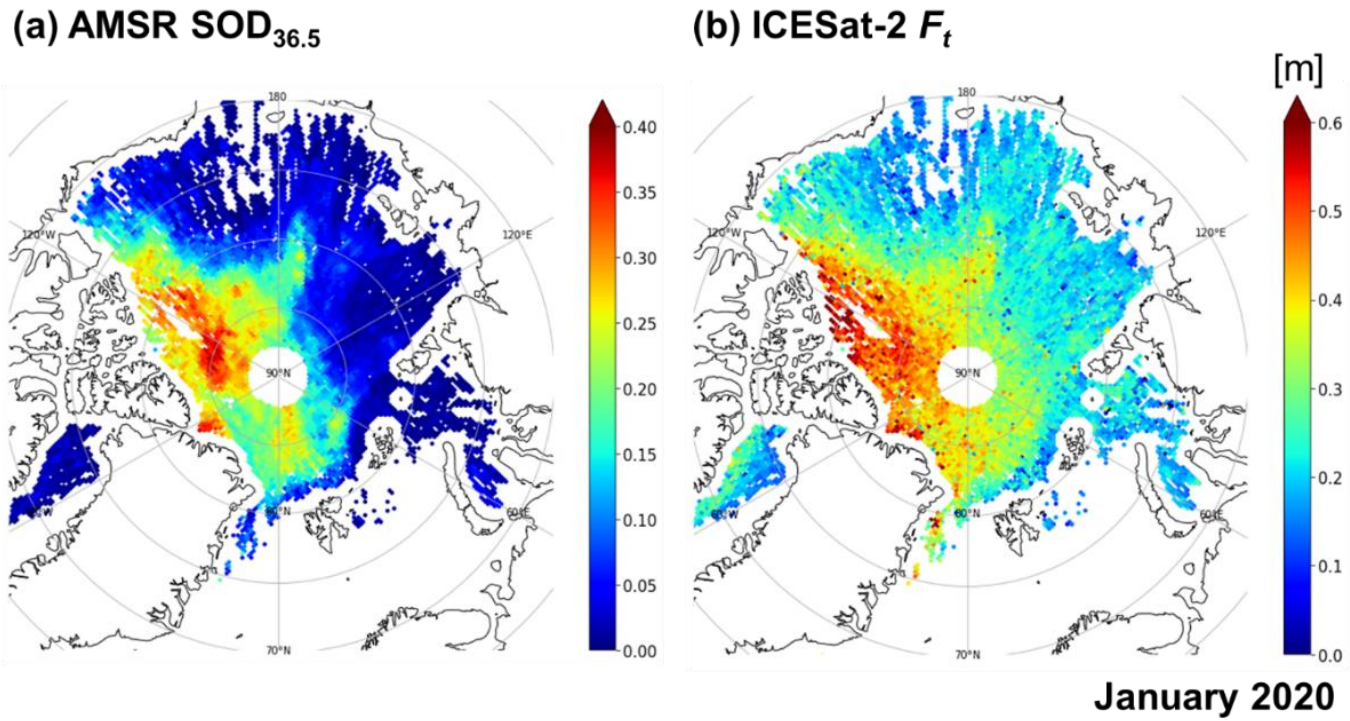

Figure 15. Geographical distributions of (a) retrieved snow-ice scattering optical depth from AMSR 36.5 GHz channel ($SOD_{36.5}$) and (b) total freeboard (F_t) obtained from ICESat-2 in January 2020. Only matched data are presented.

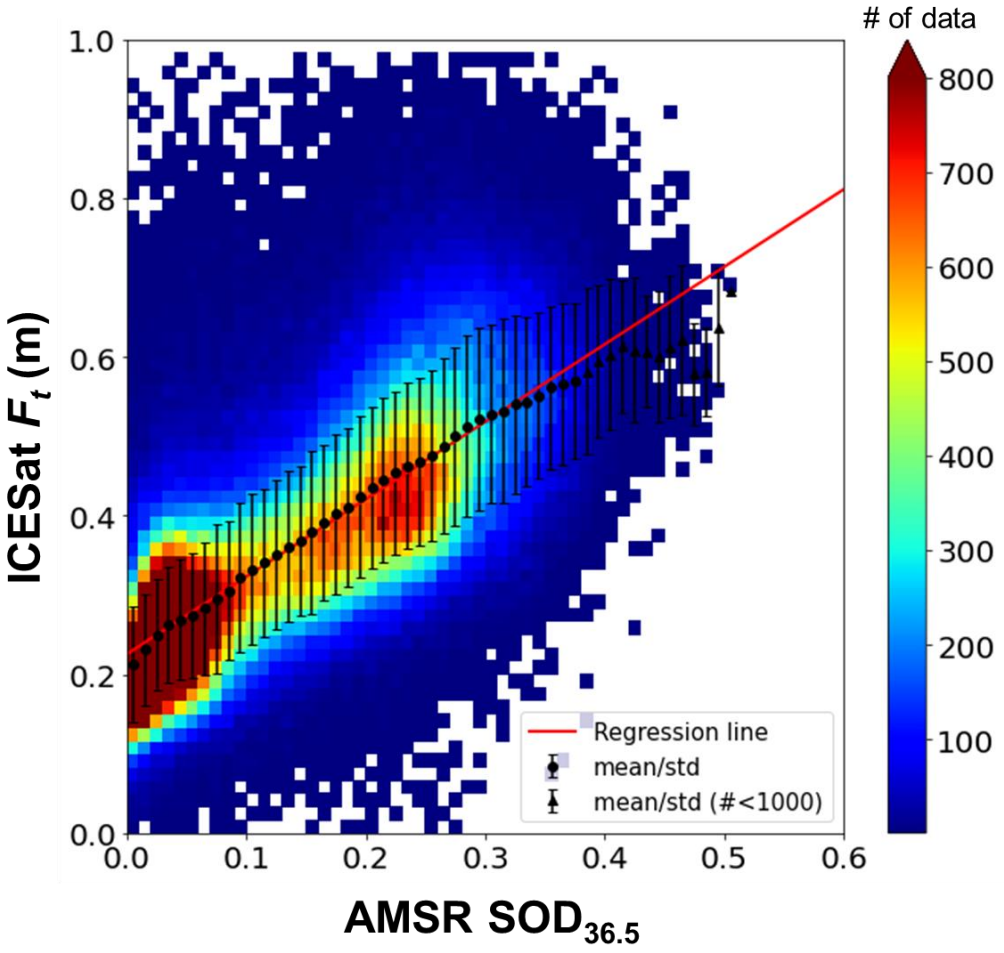

Figure 16. Two-dimensional histogram between scattering optical depth at 36.5 GHz and total freeboard. Binned analysis results are overlayed for a mean (circles/triangles) and one standard deviation (error bars). The linear fit (red solid line) is found from the binned analysis results except for values that represent less than 1000 data.

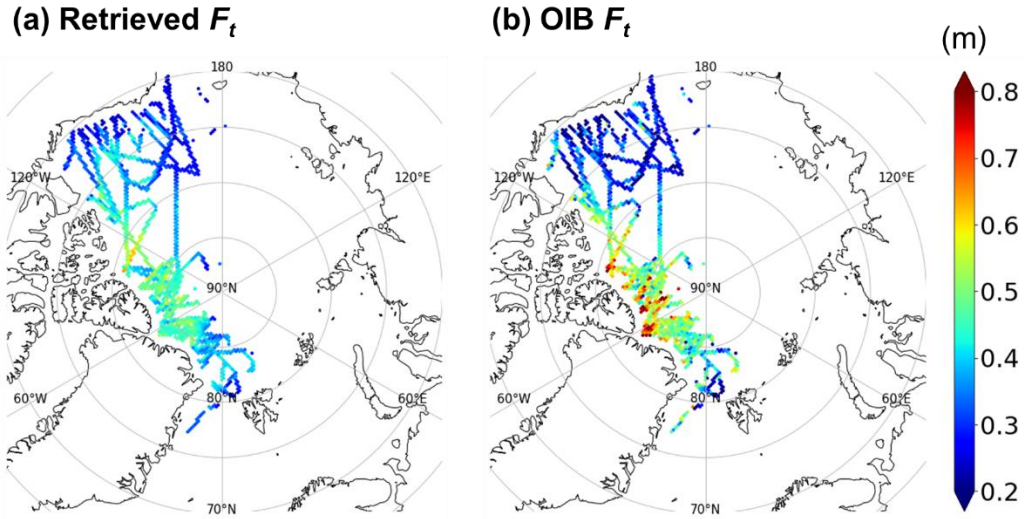

Figure 17. Geographical distributions of (a) total freeboard retrieved from AMSR scattering optical depth at 36.5 GHz and (b) OIB total freeboard for all matched data in March.

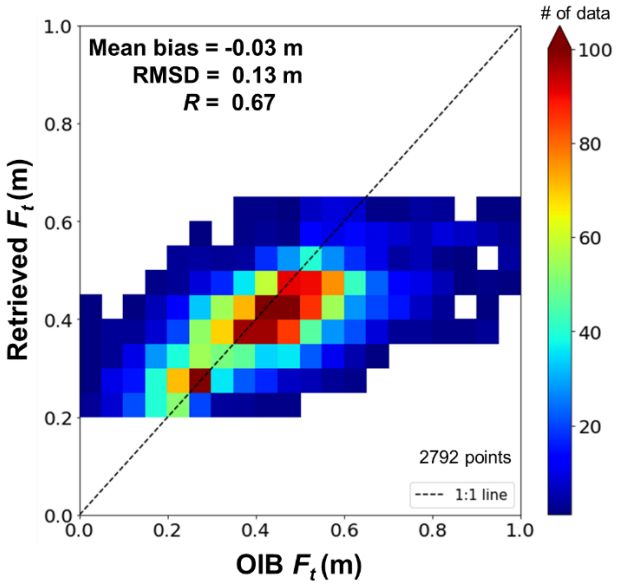

Figure 18. 2-dimensional histogram between OIB total freeboard and the total freeboard retrieved from AMSR scattering optical depth at 36.5 GHz with error statistics.

5.2.2. Snow depth from satellite passive measurements

Now, daily snow depth can be retrieved from satellite passive measurements only. The calculation was done by combining the PMW total freeboard with satellite-derived *TR* using Equation (9) with the prescribed densities. Geographical distributions of the satellite snow depth and OIB snow depth are presented in Figure 19a and Figure 19b, respectively. It seems that the satellite snow depth retrievals and OIB measurements are consistent with each other.

For quantitative validation, a 2-dimensional histogram was made with error statistics, matching 791 pairs of the retrieved h_s and OIB h_s as shown in Figure 20a. The statistics indicate that the retrieved snow depth is fairly consistent with the OIB snow depth measurements, with a near-zero bias of -1.37 cm, an RMSD of 6.26 cm, and a correlation coefficient of 0.61. To evaluate how good this product is, it is compared with the snow depth from Rostosky et al. (2018). The comparison was done for the corresponding dates of Figure 20a and the result is shown in Figure 20b as a 2-dimensional histogram. Snow depth from the PMW algorithm has a mean bias of 3.55 cm, an RMSD of 8.45 cm, and a correlation coefficient of 0.47. Based on the comparison result, it can be concluded that snow depth can be retrieved with success using the developed retrieval algorithm.

Finally, monthly Arctic basin-scale snow depth for the 2003-2020 period can

be estimated by using monthly averaged satellite interface temperatures and PMW total freeboard. After snow depth estimation for each month was done, JFM averaged fields were calculated by averaging January, February, and March snow depth fields to obtain the wintertime snow depth for each year. The evolvement of JFM averaged snow depth from the 2003 to 2020 period is presented in Figure 21. Snow depth for 2012 is not available due to a lack of AMSR data. It is shown that the snow depths over the perennial ice zone (e.g., Central Arctic and northern part of Canadian Archipelago) are deeper relative to over the seasonal ice zone (e.g., the East Siberian Sea and the Chukchi Sea). Great interannual variability of snow depth is observed in Figure 21. Deeper snow depths areas tend to be shrinking with time, probably caused by more frequent seasonal sea ice appearance.

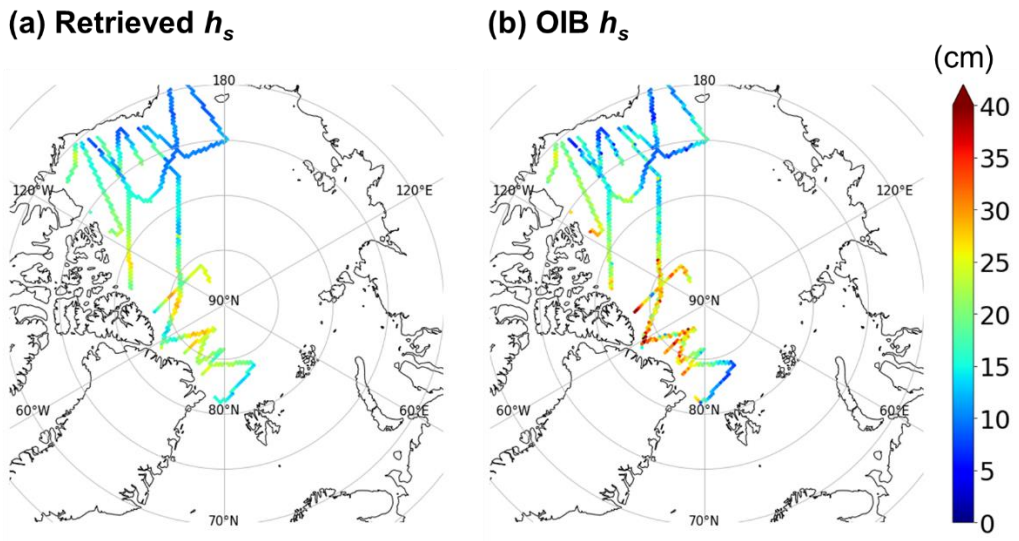

Figure 19. Geographical distributions of (a) snow depth retrieved from satellite-derived total freeboard and *TR*, and (b) OIB snow depth for all matched data in March.

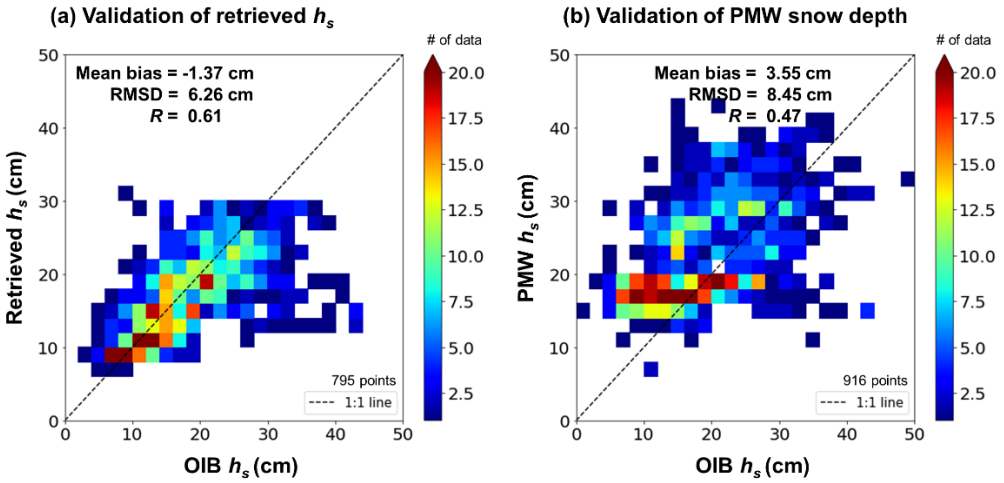

Figure 20. (a) 2-dimensional histogram between OIB snow depth and the snow depth retrieved from satellite-derived total freeboard and *TR* with error statistics. (b) Same as (a) but for the snow depth retrieved from state-of-art PMW algorithm.

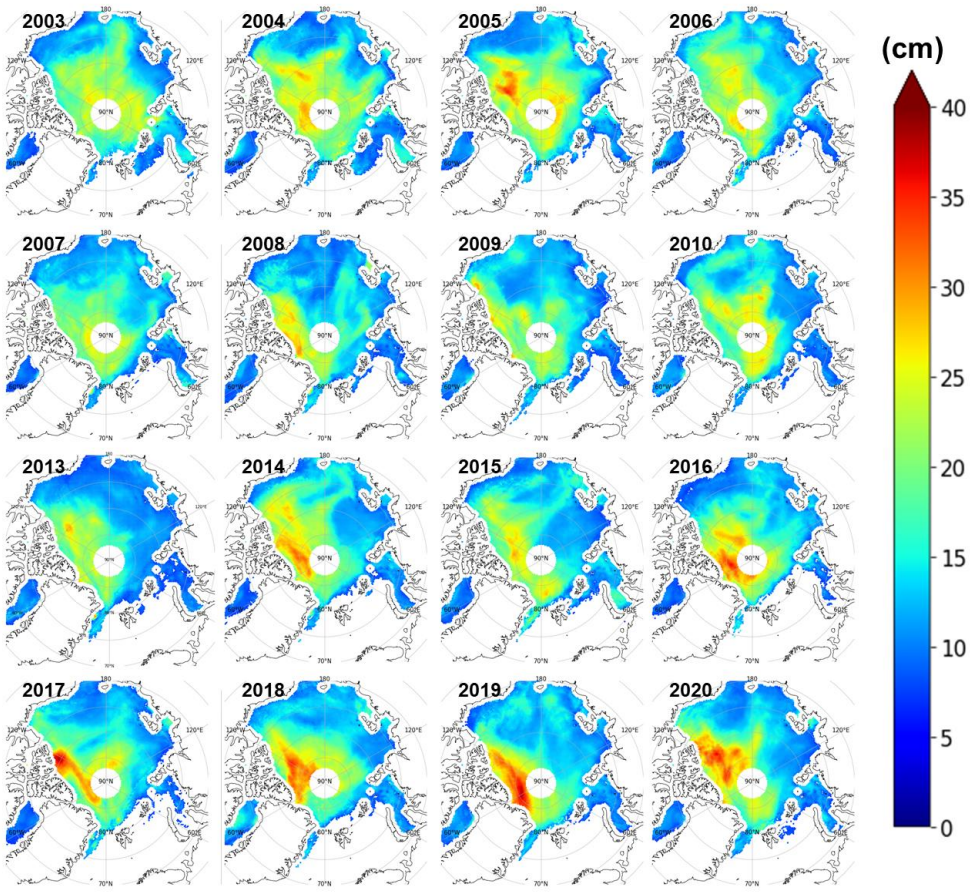

Figure 21. Geographical distributions of January-February-March averaged snow depth from 2003 to 2020.

5.2.3. Uncertainty estimation and sensitivity test

To estimate the uncertainty of retrieved snow depth, a simple propagation analysis of errors is performed, regarding the uncertainty of satellite products (*TR* and F_t) and prescribed parameters (ρ_w and ρ_i). In this study, uncertainty due to the variability of ρ_w is neglected (Kurtz and Harbeck, 2017; Hendricks et al., 2016; Ricker et al., 2014). Uncertainty of estimated snow depth can be calculated by using the following Gaussian error propagation equation.

$$E_{y,total}^2 = \sum_x E_y(x)^2 \tag{23}$$

Here, $E_{y,total}$ denotes the total uncertainty of retrieved variable y (h_s) and $E_y(x)$ denotes the uncertainty of y related to input variable x (i.e., *TR*, F_t, ρ_i, and ρ_s). In Equation (23), it is assumed that the errors of input variables are not correlated, with no systematic bias in input variables. This assumption may not be true in the real world. However, it allows us to estimate the retrieval uncertainty from satellite-derived products with a certain limit. At least, we confirmed that errors of *TR* and F_t are not correlated. The uncertainties on the right-hand side are obtained by the following equation.

$$E_y(x) = \frac{\partial y}{\partial x}\sigma_x = \lim_{\delta \to 0} \frac{y(x+\delta) - y(x)}{\delta}\sigma_x \tag{24}$$

Here, σ_x denotes the uncertainty of x and δ is set to be 10^{-6} for numerical calculation of the partial derivative. σ_{TR} is estimated to be an RMSD value between the satellite-derived *TR* and OIB derived *TR* which is 0.05. Note that OIB sea ice thickness is not a directly measured value but is calculated from F_t and h_s measurements using Equation (7) with the prescribed densities. However, it is our best reference among publicly available datasets with consideration of spatial and temporal scales. Value of σ_{Ft} is set to be 0.13 m based on the validation result in Figure 16. Uncertainties of snow and ice densities are from relevant studies (Alexandrov et al., 2010; Hendricks et al., 2016; Kern and Spreen, 2015; Ricker et al., 2014; Warren et al., 1999). Values and uncertainties of the input variables are summarized in Table 5.

Finally, uncertainties of snow depth retrievals can be estimated using Equations (23) and (24). Estimated JFM snow depth uncertainties averaged over the 2003-2020 period are presented in Figure 22a. The total uncertainty of snow depth ranges from approximately 5 cm to 15 cm and it is generally greater for the MYI region than the FYI region. From a relative point of view, snow depth uncertainty ranges from 40% over the MYI region. Over the FYI regions, the uncertainty increases up to 90% because the absolute magnitude of snow depth on FYI is very small.

To examine which error of input variables are dominant contributors in total uncertainty, the uncertainty portion is calculated for each input variable. It is revealed that *TR* is a major source of uncertainty for the coast along the North of the Canadian Archipelago-Greenland (Figure 22c) and F_t is a major source of uncertainty for the Eastern Arctic Ocean (Figure 22d). The inclusion of additional buoy measurements for improving the *TR*-temperature equation, the advance of satellite temperature retrieval algorithms, and the advance of the total freeboard retrieval algorithm can reduce uncertainties in the snow depth estimation.

In addition, we conducted a sensitivity test for each input variable to examine how the estimated snow depth is dependent on input variables. To do so, the errors of snow depth (Δh_s) due to the uncertainties of each input are calculated. Here Δh_s is defined as the difference between h_s estimated from the perturbated state and h_s estimated from a reference state (e.g., x_0; TR=0.075, F_t=0.26 m, ρ_w=1024 kg m^{-3}, ρ_i=915 kg m^{-3}, and ρ_s=320 kg m^{-3}). One can calculate Δh_s as following:

$$\Delta h_s(\sigma_x) = h_s(x_0 + \sigma_x) - h_s(x_0) \tag{25}$$

In this study, uncertainty values defined above as σ_x were used as the perturbation value. Δh_s values were calculated for negative and positive perturbations of each input variable. The results are shown in the following Table 6. It was found that all input variables are positively correlated to snow depth. In

addition to the uncertainty analysis, snow depth estimations are sensitive to *TR,* and F_t. Snow depths were relatively insensitive to the density perturbations.

Table 5. Values and uncertainties of input variables for uncertainty estimation.

	TR	F_t **(m)**	ρ_i **(kg m^{-3})**	ρ_s **(kg m^{-3})**
Value	Satellite-derived *TR*	PMW F_t	915	320
Uncertainty	0.05	0.13	20	50

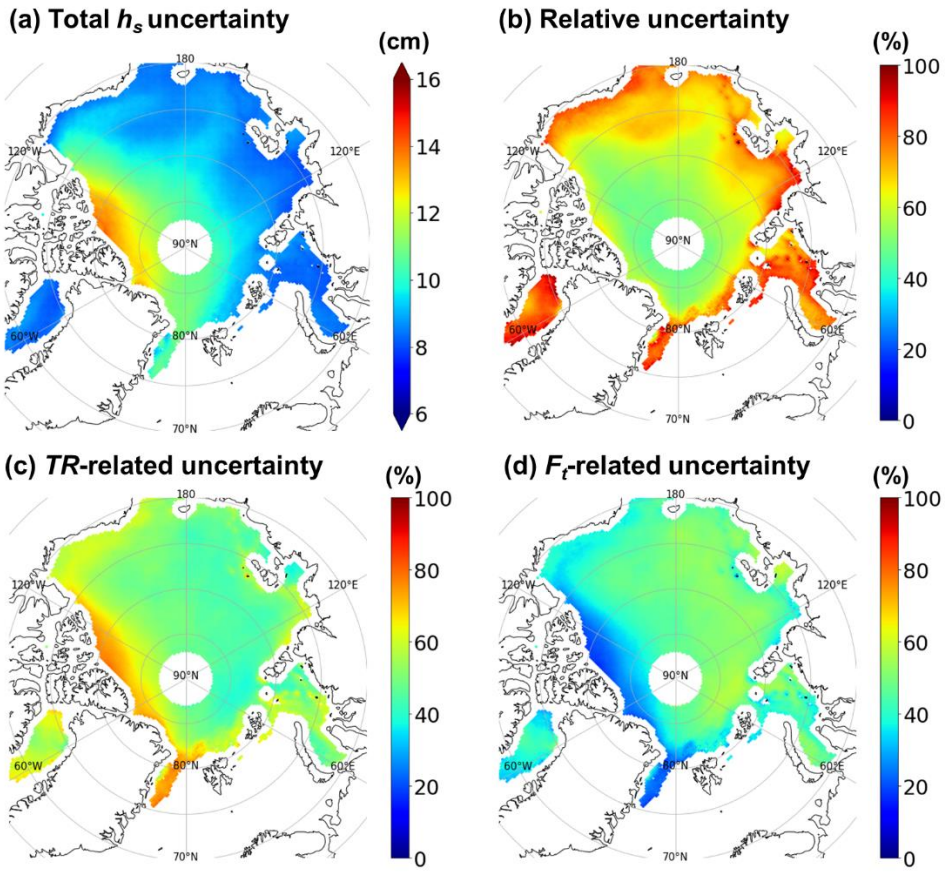

Figure 22. Geographical distributions of (a) averaged JFM snow depth uncertainty for the 2003-2020 period, (b) relative uncertainty compared to snow depth, (c) the portion of *TR*-related uncertainty, and (d) the portion of F_t-related uncertainty.

Table 6. Errors of snow depth (Δh_s) due to positive and negative perturbations of input variables.

Input variables	Δh_s	
	Negative perturbation	**Positive perturbation**
TR	-7.1 cm	4.6 cm
F_t	-6.2 cm	6.2 cm
ρ_i	-1.4 cm	1.7 cm
ρ_s	-0.3 cm	0.3 cm

5.3. Analysis of Arctic snow depth during 2003-2020 period

5.3.1. Geographical distribution

Now we have Arctic basin-scale snow depth record for the JFM months of AMSR-E and AMSR2 observation periods (i.e., the years of 2003-2020 except for 2012) (Figure 21), and this snow depth record enables us to address scientifically important questions of (1) How has the wintertime mean snow depth changed over the Arctic ocean basin compared to the W99 climatology? and (2) How the time variation of the snow depth differs from region to region during recent days? In this section, the mean and variability of wintertime snow depth are analyzed regarding the first question.

JFM averaged snow depths from the 2003 to 2020 period are presented in Figure 23a. For the mean field, pixels having less than 10 data points are neglected for calculating the statistics. The deepest snow, in between approximately 16 and 28 cm, presents over the perennial ice zone (e.g., Central Arctic and northern part of Canadian Archipelago). Snow depth is smaller over the seasonal ice zone (e.g., the northern part of Eurasia). The lowest mean snow depth is found in the Kara and Laptev Seas, ranging from approximately 7 to 16 cm. In general, snow depth on MYI is found to be deeper than that on FYI and this is also seen in other model-based and satellite-based snow depth products (Rostosky et al., 2018; Zhou et al.,

2021).

Deeper snow on MYI than FYI can be explained by the different snow accumulation periods because the snow depth is positively correlated with the snow accumulation period (Webster et al., 2014). However, a detailed relationship between the accumulation period and snow depth has not been examined yet. To examine the relationship between snow depth and accumulation period in Arctic basin-scale, freeze onset data from PMW measurements are utilized. The freeze onset is the date when the surface is maintained frozen after that day. The sea ice freeze onset product (Markus et al., 2009) is available over the 2002–2019 period distributed through the Cryosphere Research Portal (http://neptune.gsfc.nasa.gov/csb/). For comprehensive interpretation, a new variable called 'frozen days' is defined as the length of days from freeze onset to the end of the year. The geographical distribution of mean frozen days is presented in Figure 24a. As expected, frozen days for MYI are much longer than FYI. The frozen days generally range between 0 to 130 days.

In Figure 24b, a clear positive correlation is observed between two variables as shown in the 2-d histogram between mean frozen days (Figure 24a) and mean snow depth (Figure 23a). Binned analysis reveals that such relation is not linear, and the variance of mean snow depth becomes larger for longer mean frozen days. This implies that the effect of the snowfall amount is more important for MYI than

FYI. It is known that accumulation has a seasonal cycle; snow accumulates rapidly in September and October and slows down until January (Warren et al., 1999). Due to the seasonal cycle, snow depth over the MYI region affected mainly by intense snowfall in September and October rapidly increases with the frozen days, while snow depth on the FYI region affected mainly by less intense snowfall in winter shows less sensitivity to the frozen days. Therefore, the slope of the relationship between mean frozen days and mean snow depth is not constant but increases with mean frozen days.

Then, the variability of snow depth is examined. The geographical distributions of standard deviation fields from time-detrended snow depth anomalies (i.e., detrended variability) are shown in Figure 23b. It is noted that the detrended variability of snow depth generally follows the mean snow depth fields. Relatively large interannual variability of JFM snow depth over MYI areas is observed, while snow depth on FYI has a smaller and smoother interannual variability. The snow depth variability over MYI shows a mean value of 3.97 cm and a standard deviation of 0.95 cm, approximately. It ranges between approximately 3 to 6 cm, which lies between previously reported values from W99 (4.6 to 6.2 cm) and values from snow accumulation models (2 to 3 cm) (Zhou et al., 2021).

To figure out whether snow depth has reduced or increased relative to W99

snow depth climatology (Figure 23c), relative JFM mean snow depth compared to W99 climatology was calculated as shown in Figure 23d. A significant decrease in snow depth was found over the FYI region. Especially, snow depth reduced to approximately 40% level of the W99 climatology over the Beaufort and Chukchi seas (18.3 cm decrease in absolute value). This snow depth reduction is consistent with the reported value by Webster et al. (2014). By comparing the W99 climatology with the OIB measured snow depth during the 2009-2013 period, they found that the snow depth has decreased from 32.86 cm to 14.56 cm (decreased to 44% level) in the Beaufort and Chukchi seas. Snow depth reduction was relatively small in the case of snow depth on MYI, however, it has been reduced to approximately 55 to 80% level of W99 climatology (6 cm to 10 cm decrease in absolute value). This result indicates that W99 snow depth climatology base on buoy measurements in the 1954-1991 period is no longer valid for the present day.

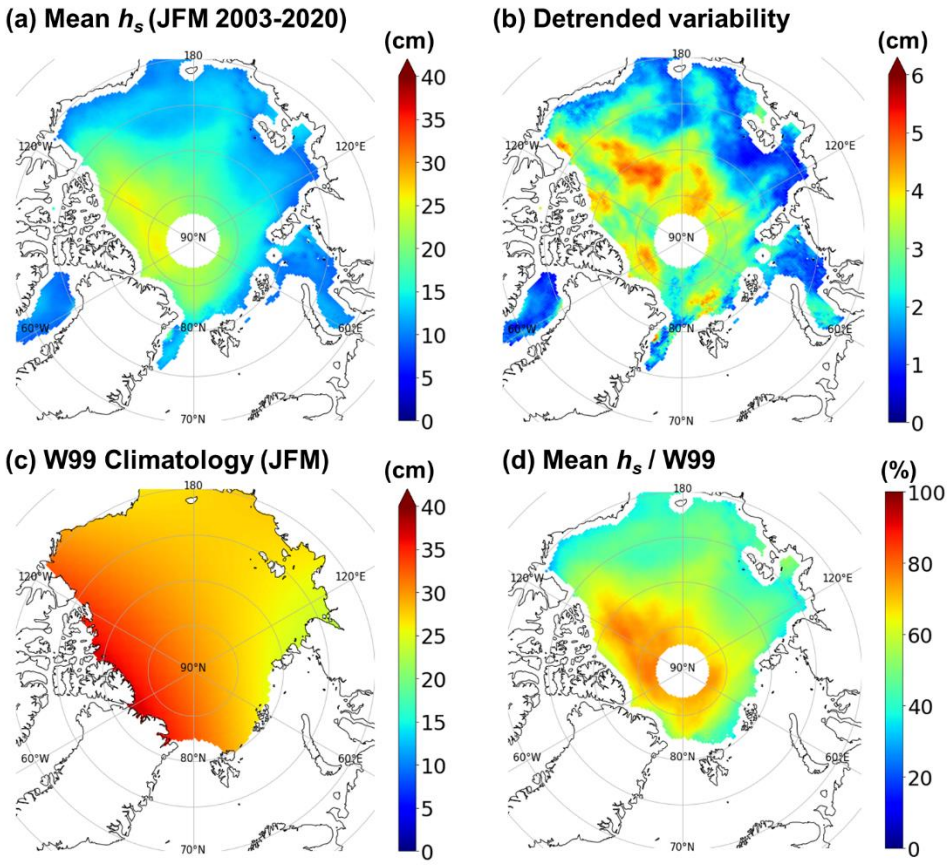

Figure 23. Geographical distributions of averaged (a) JFM mean snow depth for the 2003-2020 period, (b) corresponding detrended variability, (c) W99 snow depth climatology, and (d) the ratio between the mean snow depth and W99 climatology.

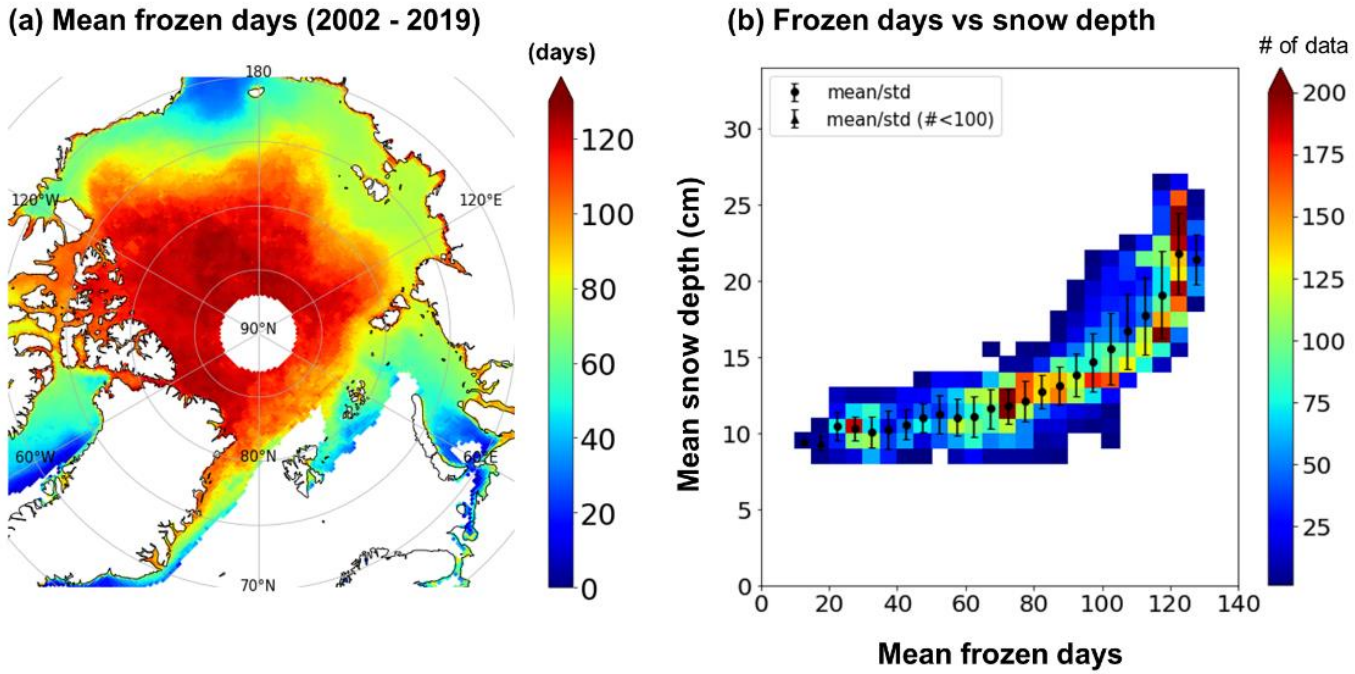

Figure 24. (a) Geographical distributions of (a) mean frozen days and (b) relationship between mean frozen days and mean snow depth overlayed with binned analysis result.

5.3.2. Temporal variation

To answer the second question regarding the temporal variation of snow depth, trends of snow depth are calculated and presented in Figure 25a. As before, pixels having less than 10 data points are neglected for calculating the statistics. The obtained result indicates that snow depth trends are highly variable by region or sea ice type.

Statistically significant negative trends in snow depth (-0.29 cm/yr on average; up to -0.50 cm/yr) on FYI near the Laptev Sea to the Central Arctic Ocean and the northern part of the East Siberian Sea (bluish shaded and dotted area in Figure 25a). Those regions are generally consistent with the regions where MYI turns into FYI. Considering that snow depth on MYI is greater than snow depth on FYI, the significant negative trends are closely related to the sea ice type transition. Besides, negative trends over FYI would also be related to the delayed freeze-up dates due to Arctic warming, shortening the snow accumulation period on FYI.

Statistically significant positive trends in snow depth (0.43 cm/yr on average; up to +0.70 cm/yr) are observed over MYI near the northern part of Greenland and the Canadian Archipelago (reddish shaded and dotted area in Figure 25a). The positive trend is likely to be related to increased autumn and winter precipitation,

likely caused by more frequent cyclone occurrences (Graham et al., 2019; Kwok et al., 2020), because Arctic cyclone activity is closely related to snowfall on sea ice (Serreze et al., 2012; Webster et al., 2019).

To compare this result with others, reanalysis-based snow depth reconstruction (SnowModel-LG; Liston et al., 2020) data are introduced. SnowModel-LG accumulates and redistributes snowfall from atmospheric reanalysis in a Lagrangian framework using satellite-derived ice motion vectors (Liston et al., 2020) and it includes physical processes associated with snow layer (e.g., blowing snow, snowpack metamorphosis, and compression). This study utilizes JFM averaged fields of SnowModel-LG forced with ERA5 and sea ice motion vectors from the NSIDC (Tschudi et al., 2019b). Snow depth trends of the SnowModel-LG were calculated for the 2003-2018 periods because SnowModel-LG data are available up to 2018. SnowModel-LG shows a similar geographical distribution of snow depth trends but with a greater magnitude of negative trends and with less organized positive trends over MYI (Figure 25b). However, over a longer period from 1991-2015, significant positive snow depth trends in agreement with this study are noted over the northern part of the Canadian Archipelago and Greenland in reanalysis-based snow depth reconstructions including SnowModel-LG (Zhou et al., 2021).

To see snow depth distribution in detail, probability distribution functions

(PDFs) of mean snow depth for each year are made as in Figure 26a. Reduced snow depth compared to W99 snow depth climatology can be clearly observed. By observing snow depth PDF for the whole period (black solid line), a bimodal distribution of snow depth is observed with peaks at approximately 12.5 cm and 22 cm, and two modes correspond to snow depth on FYI and MYI, respectively. However, we can observe that snow depth distribution has significantly changed during the 2003-2020 period by comparing PDFs for the first 5-year period (2003-2007, blue solid line) and the last 5-year period (2016-2020, red solid line). It is observed that snow depth distribution becomes single mode with a peak at approximately 13 cm and the maximum range of snow depth has increased. These PDFs suggest that the snow depth on FYI has become the dominant contributor to the overall snow depth over the Arctic basin in more recent years and the thickest snow on MYI has become thicker.

The mean snow depth time series for each ice type is shown in Figure 26b. MYI snow depth shows a slightly increasing trend, while there is not much difference for FYI snow depth and overall snow depth. The mean snow depth time series is consistent with the PDF analysis results: FYI is the dominant sea ice type over the Arctic Ocean and snow depth on FYI did not change significantly. This seems to be contradicted with the significant negative snow depth trend in Figure 25a. However, it is not a contradiction because the significant negative trend is

due to from sea ice type transition: thick snow on MYI is replaced by thin snow on FYI. This becomes clear if we look at the time series of snow depth for regions showing statistically significant positive and negative trends in Figure 27a. Snow depths for the two regions were close to each other initially in 2003 which may represent snow depth on MYI. Moreover, the regions showing significant negative trends well correspond with the regions showing significant negative trends of MYI fraction (Figure 27b).

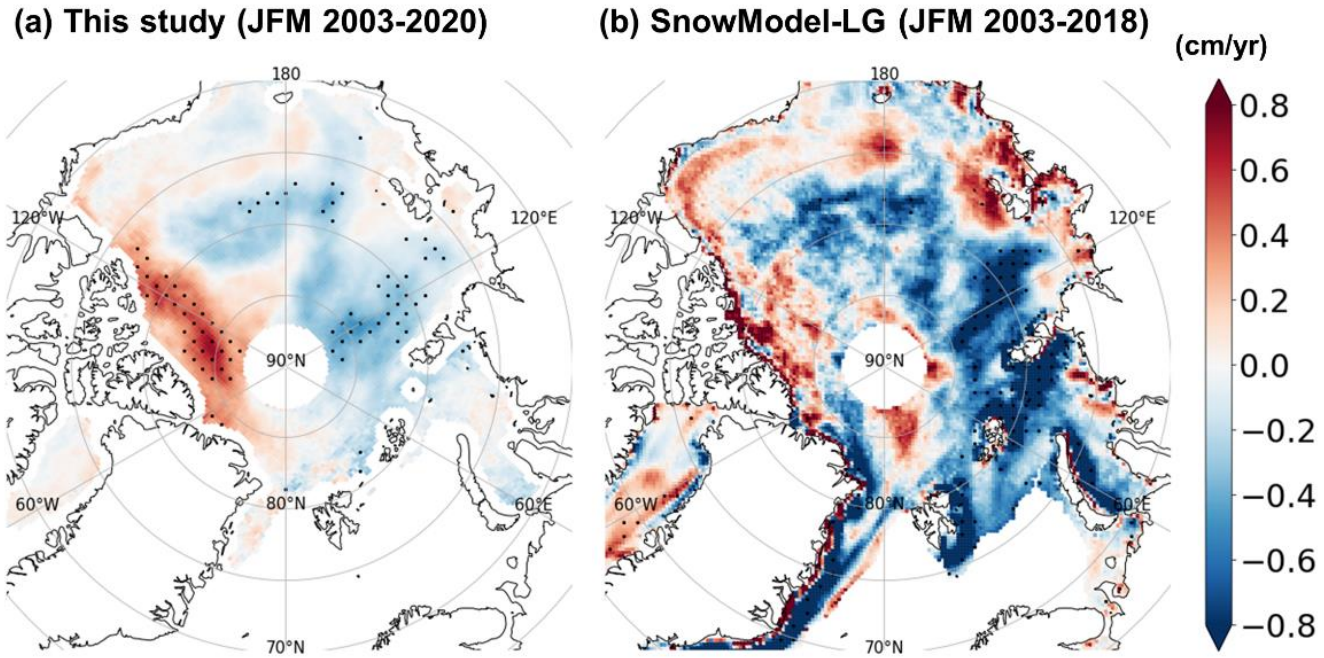

Figure 25. Geographical distributions of JFM averaged snow depth trend of (a) snow depth produced in this study (2003-2020 period) and (b) snow depth from the SnowModel-LG (2003-2018 period). The dotted area indicates the region where the linear trend is significant over 95% confidence level.

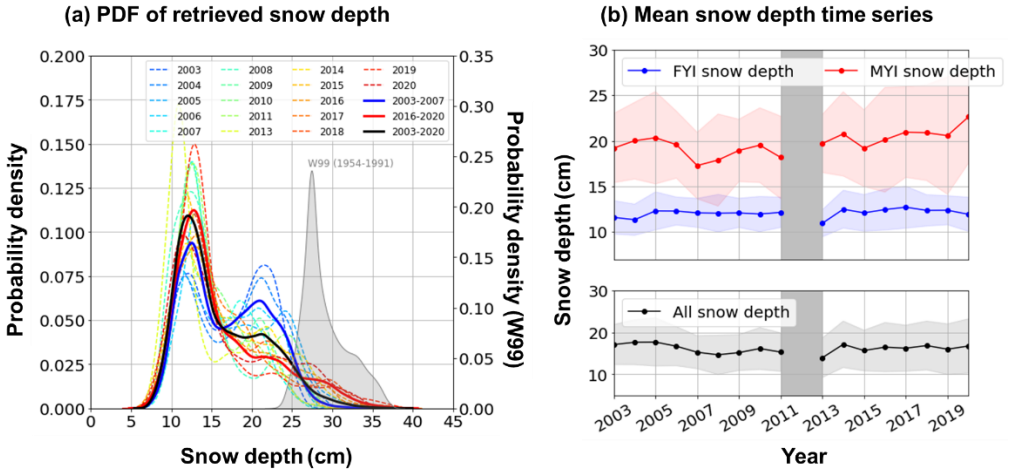

Figure 26. (a) Time evolution of retrieved snow depth distribution. W99 climatology is illustrated in the grey-shaded probability distribution function (PDF). (b) Time series of mean snow depth for each ice type. Shade denotes standard deviation.

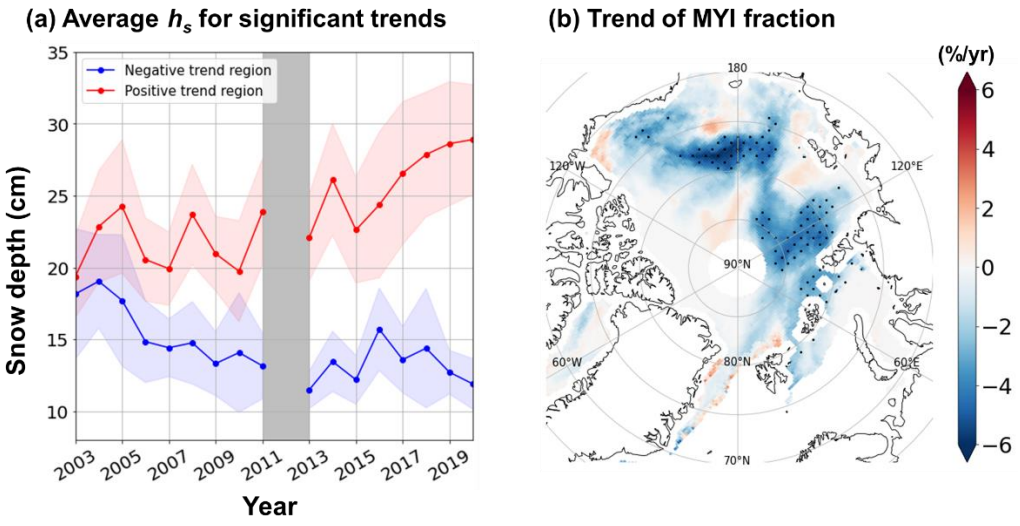

Figure 27. (a) Time series of mean snow depth for regions where snow depth trend is significant. Shade denotes standard deviation. (b) The trend of MYI fraction.

6. Conclusions and discussion

The snow on Arctic sea ice is an important element in the Earth's climate system. It dampens direct heat and mass exchange between the atmosphere and the ocean, and it reflects a large amount of incoming solar energy. Considering these, observing the snow depth on Arctic sea ice is essential for improving our understanding of the Arctic weather and climate. However, the estimation of the Arctic snow depth from PMW measurements has been a challenging task for the satellite community, especially over the MYI region.

In this study, a novel satellite retrieval algorithm for the wintertime Arctic basin-scale snow depth was developed based on the hydrostatic balance and thermodynamic steady-state of a snow-ice system. The key concept of this algorithm is to estimate snow depth and ice thickness simultaneously from the thickness ratio *TR* which is defined as the ratio between snow depth and sea ice thickness, and the total freeboard measurements.

The *TR* is estimated from the vertical thermal structure of the snow-ice system (i.e., snow top temperature and snow-ice interface temperature) which can be resolved from satellite infrared and microwave radiometer measurements during wintertime. To do so, the empirical relationship between *TR* and the interface temperatures (i.e., *TR*-temperature equation) was obtained from buoy

data analysis. Total freeboard was estimated from satellite PMW measurements rather than satellite altimeter measurements to obtain Arctic basin-scale total freeboard. PMW total freeboard was estimated by using the snow-ice scattering optical depth at 36.5 GHz channel ($SOD_{36.5}$) as a predictor. It was found that snow depth retrieved from *TR* and PMW total freeboard was consistent with OIB snow depth.

Using the developed algorithm, wintertime snow depth records for the 2003-2020 period were estimated from AVHRR and AMSR measurements. Currently, most of the satellite snow depth products rely upon the OIB dataset showing differences from product to product (Kwok et al., 2017), which implies the OIB-dependent snow depth should inherit potential bias within certain OIB products. On the other hand, the snow depth data record provided by this study is a unique dataset because the suggested snow depth estimation method is independent of the OIB dataset. Although the suggested method is independent of OIB data, good consistency in snow depth between this study and OIB (Kurtz et al., 2015) was found, demonstrating that a reliable snow depth can be estimated from satellite radiometer measurements. Flowchart summarizing this study is provided for comprehensive understanding in Figure 28.

Spatio-temporal variability of the produced Arctic snow depth record was analyzed. In general, snow depth on MYI was greater than snow depth on FYI,

which is related to the length snow accumulation period. To examine such relation in detail, the relationship between mean snow depth and frozen days was analyzed, revealing that they are positively correlated. However, the relationship was not linear but the sensitivity of mean snow depth to frozen days was greater for the longer frozen days.

This study revealed that the mean snow depth is significantly reduced compared to the W99 snow depth climatology over both MYI and FYI regions. This snow depth reduction has been reported by other studies as well for limited areas or time (Webster et al., 2014; Kwok et al., 2020). Although it is hard to consider that the W99 for the 1954-1991 period is valid over the Arctic Ocean for recent decades, it is still used for satellite ice thickness retrieval with a modification (Sallila et al., 2019). Many studies modified W99 (hereafter referred to as mW99) by dividing W99 by a factor of 2 over FYI based on a report by Kurtz and Farrell (2011).

However, it has been suggested that mW99 introduces systematic bias in sea ice thickness estimation (Kwok et al., 2020; Stroeve et al., 2020; Shi et al., 2020). The overestimated mW99 snow depth will likely cause underestimation (overestimation) of ice thickness when using lidar (radar) altimeter measurements (Shi et al., 2020). Such underestimation and overestimation due to mW99 were demonstrated by a recent study that revealed a significant bias between the ice

thicknesses estimated from lidar (i.e., ICESat) and radar (i.e., CryoSat-2) altimeters (Kim et al., 2020). In conclusion, the consideration of using satellite-based snow depth for sea ice thickness retrieval is desirable.

An interesting snow depth trend with spatially different patterns is noted. A positive snow depth trend was found over the western Arctic while a negative trend was found over the Eastern Arctic. It is thought that the negative trend is related to sea ice type transition and delayed freeze onset (Webster et al., 2014) and positive trends are thought to be related to increased snowfall due to more frequent intrusion of Arctic cyclones through the Atlantic Ocean (Kenigson and Timmermans, 2021) and Pacific Ocean (Tachibana et al., 2019). Regarding the ice thickness retrieval, these regional trends of snow depth suggest that ice thickness trends derived from the fixed mW99 climatology most likely contain erroneous regional trends (Shi et al., 2020).

Another consequence of snow depth change would be an influence on sea ice loss associated with the insulation effect of the snow layer. Snow is a good thermal insulator due to its low thermal conductivity, and it controls conductive heat flux from the ocean to the atmosphere. Therefore, thickened snow layer prevents the rapid growth of sea ice during winter by dampening the uptake of thermal energy by the atmosphere from the ocean. Consequently, thickened snow cover can result in thinner ice (Ledley, 1991). The indirect evidence of this is given as the trends

of snow depth portion in total snow-ice thickness (Figure 29). Thinner sea ice has less chance to survive successive summer because thinner ice requires less energy to melt away. Besides, dynamical sea ice loss is as important as the thermodynamic process. Thinner ice is more likely to break up into small ice floes with increased mobility. On top of this condition, recently increased cyclone intrusion to Arctic weekends Beaufort High (Moore et al., 2018) promoting sea ice export (Rigor et al., 2002). As a result, the open ocean area increases during the melting period and causes a warm and moist Arctic atmosphere (Kim et al., 2019; Higgins and Cassano, 2009). Rapid warming of the Arctic region results in the northward shift of the tropospheric polar vortex (Kenigson and Timmermans, 2021) promoting more favorable conditions for cyclone intrusion. These changes are linked to snow depth increase over the MYI region which can form a sea ice loss feedback loop (Figure 30). Further investigation on this suggested feedback mechanism is needed, especially taking into consideration of cyclone intrusion timing (Webster et al., 2019), ocean heat transport (Auclair and Tremblay, 2018), moisture transport (Bintanja et al., 2020), and surface longwave radiative effect of cloud (Yeo et al., 2018).

The obtained Arctic basin-scale snow depth records can be used for improving the atmospheric reanalysis data and Arctic climate prediction. Most Arctic climate research utilizes reanalysis data because there are not enough

observations available over the Arctic. For instance, anomalous surface turbulent heat flux was used as an indicator to investigate causality between sea ice loss and mid-latitude cold surges during winter (Blackport et al., 2019). However, the majority of atmospheric reanalysis models are missing the snow layer on sea ice in the surface physics process which is a crucial factor for the surface energy balance (ECMWF, 2007; ECMWF, 2016; Batrak and Müller, 2019). The conductive heat flux through sea ice is balanced with other energy fluxes above the snow surface. The missing snow cover makes conductive heat flux be overestimated, resulting in a significant warm bias of surface temperature (Batrak and Müller, 2019; Wang et al., 2019). Therefore, reanalysis models must take into account snow depths for more realistic surface energy fluxes. To do so, appropriate snow depth data should be assimilated into the model. Besides, climate models require realistic initial conditions for the improved climate prediction. The snow depth records produced in this study can be used for such purposes.

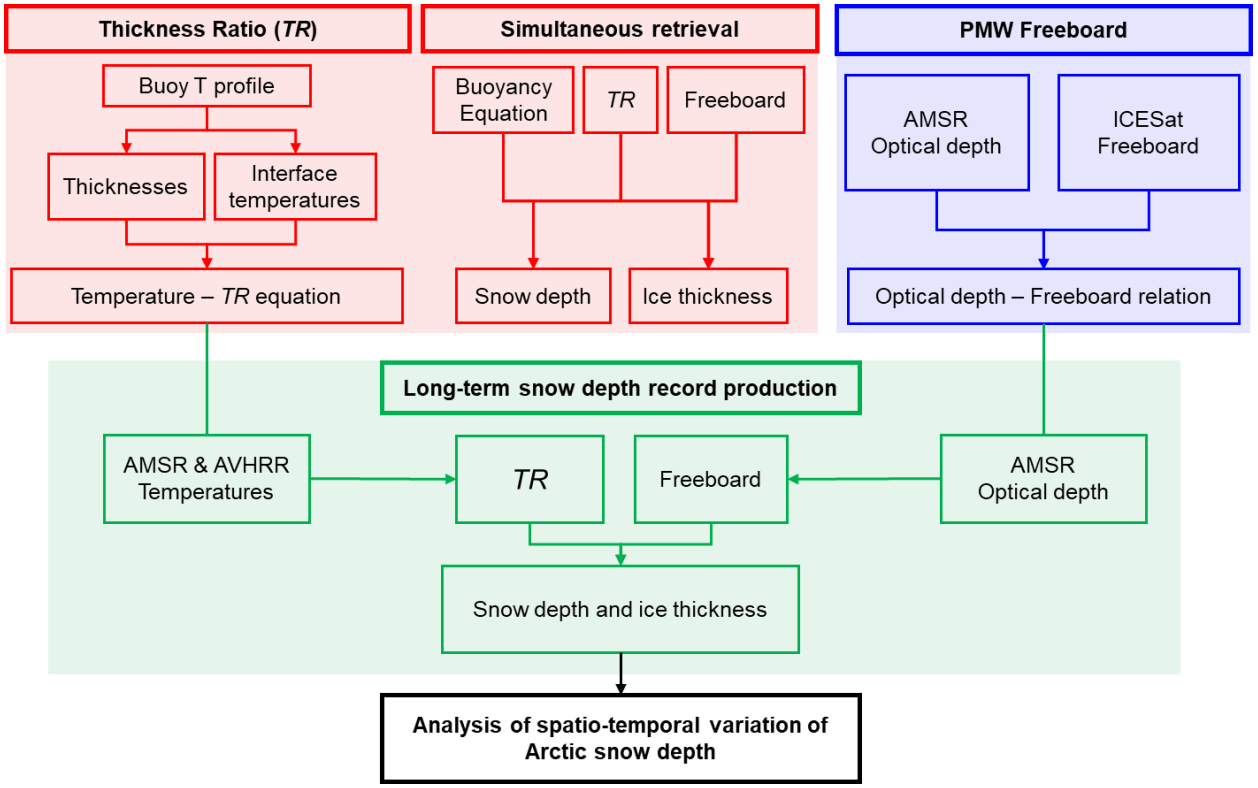

Figure 28. Flow chart of this study: (Red box) development of snow depth retrieval algorithm, (Blue box) estimation of sea ice freeboard from satellite PMW measurements, and (Green box) production of long-term snow depth record.

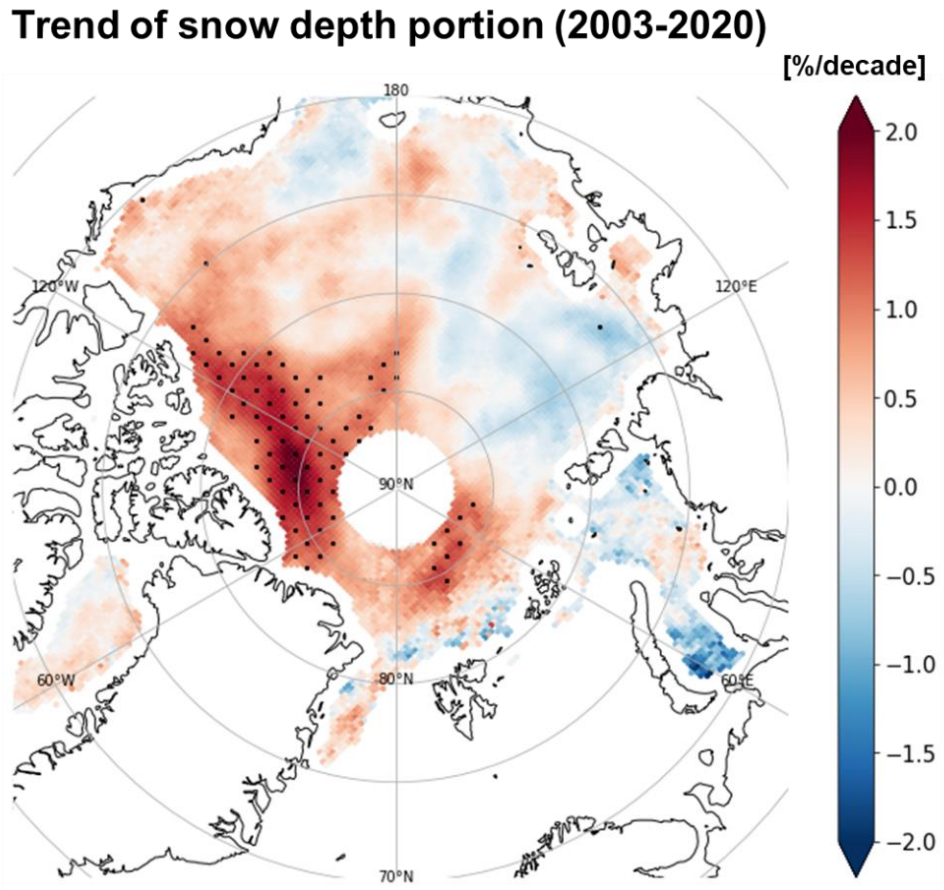

Figure 29. Geographical distribution of the decadal trend of snow depth portion in the total snow-ice thickness for the 2003-2020 period. The dotted area indicates the region where the linear trend is significant over 95% confidence level.

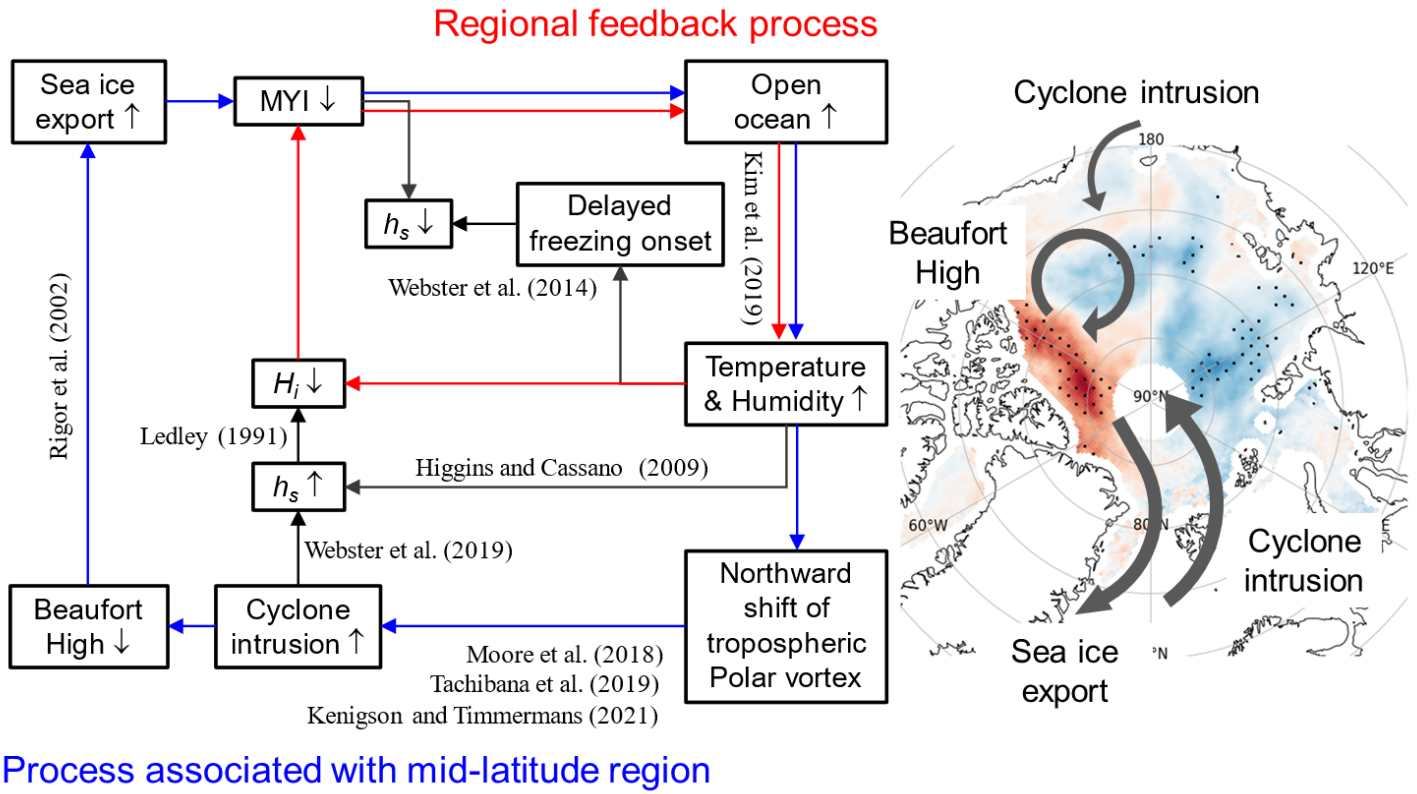

Figure 30. Diagram of the snow depth related feedback mechanisms over the Arctic Ocean.

References

Alexandrov, V., Sandven, S., Wahlin, J., and Johannessen, O. M.: The relation between sea ice thickness and freeboard in the Arctic, *The Cryosphere*, **4**, 373-380, doi: 10.5194/tc-4-373-2010, 2010.

Andersen, J. K., Andreassen, L. M., Baker, E. H., Ballinger, T. J., et al.: The Arctic, *Bull. Am. Meteorol. Soc.*, **101**, S239-S286, doi: 10.1175/BAMS-D-20-0086.1, 2020.

Armitage, T. W. K., and Ridout, A. L.: Arctic sea ice freeboard from AltiKa and comparison with CryoSat-2 and Operation IceBridge, *Geophys. Res. Lett.*, **42**, 6724–6731, doi: 10.1002/2015GL064823, 2015.

Auclair, G., and Tremblay, L. B.: The role of ocean heat transport in rapid sea ice declines in the community Earth system model large ensemble, *J. Geophys. Res.-Oceans*, **123**(12), 8941-8957, doi: 10.1029/2018JC014525, 2018.

Batrak, Y., and Müller, M.: On the warm bias in atmospheric reanalyses induced by the missing snow over Arctic sea-ice, *Nat. Commun.*, **10**, 4170, doi: 10.1038/s41467-019-11975-3, 2019.

Bintanja, R., van der Wiel, K. van der Linden, E. C., Reusen, J., Bogerd, L., Krikken, F., and Selten, F. M.: Strong future increases in Arctic precipitation variability linked to poleward moisture transport, *Sci. Adv.*, **6**(7), eaax6869, doi: 10.1126/sciadv.aax6869, 2020.

Blackport, R., Screen, J.A., van der Wiel, K., and Bintanja, R.: Minimal influence of reduced Arctic sea ice on coincident cold winters in mid-latitudes, *Nat. Clim. Chang.*, **9**, 697–704, doi: 10.1038/s41558-019-0551-4, 2019.

Braakmann-Folgmann, A., and Donlon, C.: Estimating snow depth on Arctic sea ice using satellite microwave radiometry and a neural network, *The Cryosphere*, **13**, 2421–2438, doi: 10.5194/tc-13-2421-2019, 2019.

Brucker, L., and Markus, T.: Arctic-scale assessment of satellite passive microwave-derived snow depth on sea ice using Operation IceBridge airborne data, *J. Geophys. Res.-Oceans*, **118**(6), 2892–2905, doi: 10.1002/jgrc.20228, 2013.

Cavalieri, D. J., Gloersen, P., and Campbell, W. J.: Determination of Sea Ice Parameters with the NIMBUS-7 SMMR, *J. Geophys. Res.*, **89**(D4), 5355-5369, 1984.

Cavalieri, D. J., Parkinson, C. L., Gloersen, P., Comiso, J. C., and Zwally, H. J.: Deriving long-term time series of sea ice cover from satellite passive-microwave multisensory data sets, *J. Geophys. Res.*, **104**(C7), 15803-15814. doi: 10.1029/1999JC900081, 1999.

Comiso, J. C.: Characteristics of Arctic Winter Sea Ice from Satellite Multispectral Microwave Observations, *J. Geophys. Res.*, **91**(C1), 975-994, 1986.

Comiso, J. C., Cavalieri, D. J., and Markus, T.: Sea ice concentration, ice temperature, and snow depth using AMSR-E data, *IEEE Trans. Geosci. Remote Sens.*, **41**(2), 243–252, doi: 10.1109/TGRS.2002.808317, 2003.

Cox, G. F. N., and Weeks, W. F.: Salinity variations in sea ice, *J. Glaciol.*, **13**(67), 109–120, doi: 10.3189/S0022143000023418, 1974.

Dybkjær, G., Højer, J., Tonboe, R., and Olsen, S.: Report on the documentation and description of the new Arctic Ocean dataset combining SST and IST,

NACLIM Deliverable, D32.28, 2014. (Available at https://naclim.cen.uni-hamburg.de/index.php?id=2224)

European Centre for Medium-range Weather Forecasts (ECMWF): Part IV: Physical Processes, *IFS Documentation – Cy41r2*, 1-213, doi: 10.21957/tr5rv27xu, 2016.

European Centre for Medium-range Weather Forecasts (ECMWF): Part IV: Physical Processes, *IFS Documentation – Cy31r1*, 1-155, doi: 10.21957/orqi6pqsa, 2017.

Francis, J., and Vavrus, S. J.: Evidence for a wavier jet stream in response to rapid Arctic warming, *Env. Res. Lett.*, **10**, 014005, doi: 10.1088/1748-9326/10/1/014005, 2015

Graham, R. M., Itkin, P., Meyer A., et al.: Winter storms accelerate the demise of sea ice in the Atlantic sector of Arctic Ocean, *Scientific Report*, **9**, 9222, doi: 10.1038/s41598-019-45574-5, 2019.

Grosfeld, K., Treffeisen, R., Asseng, J., Bartsch, A., Bräuer, B., Fritzsch, B., Gerdes, R., Hendricks, S., Hiller, W., Heygster, G., Krumpen, T., Lemke, P., Melsheimer, C., Nicolaus, M., Ricker, R., and Weigelt, M.: Online sea-ice knowledge and data platform <www.meereisportal.de>, *Polarforschung, Bremerhaven, Alfred Wegener Institute for Polar and Marine Research & German Society of Polar Research*, **85**(2), 143-155, doi:10.2312/polfor.2016.011, 2016.

Guerreiro, K., Fleury, S., Zakharova, E., Rémy, F., and Kouraev, A.: Potential for estimation of snow depth on Arctic sea ice from CryoSat-2 and SARAL/AltiKa missions, *Remote Sens. Environ.*, **186**, 339–349, doi:

10.1016/j.rse.2016.07.013, 2016.

Hendricks, S., Ricker, R., and Helm, V.: User Guide – AWI CryoSat-2 sea Ice thickness data product (v1.2), doi: 10013/epic.48201, 2016.

Hersbach, H., Bell, B., Berrisford, P., Hirahara, S., Horányi, A., Muñoz Sabater, J., et al.: The ERA5 global reanalysis, *QJRMS*, **146**(730), 1999–2049, doi: 10.1002/qj.3803, 2020.

Higgins, M. E., and Cassano, J. J.: Impacts of reduced sea ice on winter Arctic atmospheric circulation, precipitation, and temperature, *J. Geophys. Res.-Atmos.*, **114**(D16), D16107, doi: 10.1029/2009JD011884, 2009.

Japan Aerospace Exploration Agency (JAXA): Intercomparison results between AMSR2 and TMI/AMSR-E/GMI (AMSR2 Version 2.0), 2015. (available at https://suzaku.eorc.jaxa.jp/GCOM_W/materials/product/150326_AMSR2_XcalResults.pdf; last accessed: October 2018).

Kenigson, J. S., and Timmermans, M.-L.: Arctic cyclone activity and the Beaufort high, *J. Clim.*, **34**(10), 4119-4127, doi: 10.1175/JCLI-D-20-0771.1, 2021.

Kern, S. and Spreen, G.: Uncertainties in Antarctic sea-ice thickness retrieval from ICESat, *Ann. Glaciol.*, **56**, 107–119, doi: 10.3189/2015AoG69A736, 2015.

Kilic, L., Tonboe, R. T., Prigent, C., and Heygster, G.: Estimating the snow depth, the snow-ice interface temperature, and the effective temperature of Arctic sea ice using Advanced Microwave Scanning Radiometer 2 and ice mass balance buoy data, *The Cryosphere*, **13**, 1283–1296, doi: 10.5194/tc-13-1283-2019, 2019.

Kim, J. M., Sohn, B. J., Lee, S. M., Tonboe, R. T., Kang, E. J., and Kim, H. C.:

Differences between ICESat and CryoSat-2 sea ice thicknesses over the Arctic: Consequences for analyzing the ice volume trend, *J. Geophys. Res.-Atmos.*, **125**(22), e2020JD033103. doi: 10.1029/2020JD033103, 2020.

Kim, K.-Y., Kim, J-Y., Kim, J., Yeo, S., Na, H., Hamlington, B. D., and Leben, R. R.: Vertical feedback mechanism of winter Arctic amplification and sea ice loss, *Sci. Rep.*, **9**, 1184, doi: 10.1038/s41598-018-38109-x, 2019.

Kug, J.-S., Jeong, J.-H., Jang, Y.-S., Kim, B.-M., Folland, C. K., Min, S.-K., and Son, S.-W.: Two distinct influences of Arctic warming on cold winters over North America and East Asia, *Nature Geosci.*, **8**, 759–762, doi: 10.1038/ngeo2517, 2015.

Kurtz, N. T. and Farrell, S. L.: Large-scale surveys of snow depth on Arctic sea ice from Operation IceBridge, *Geophys. Res. Lett.*, **38**, L20505, doi: 10.1029/2011GL049216, 2011.

Kurtz, N. T., Farrell, S. L., Studinger, M., Galin, N., Harbeck, J. P., Lindsay, R., Onana, V. D., Panzer, B., and Sonntag, J. G.: Sea ice thickness, freeboard, and snow depth products from Operation IceBridge airborne data, *The Cryosphere*, **7**, 1035–1056., doi: 10.5194/tc-7-1035-2013, 2013.

Kurtz, N. and Harbeck, J.: CryoSat-2 Level-4 Sea Ice Elevation, Freeboard, and Thickness, Version 1, *Boulder, Colorado USA. NASA National Snow and Ice Data Center Distributed Active Archive Center*, doi: 10.5067/96JO0KIFDAS8, 2017.

Kurtz, N., M. Studinger, J. Harbeck, V. Onana, and D. Yi.: IceBridge L4 Sea Ice Freeboard, Snow Depth, and Thickness, Version 1, *Boulder, Colorado USA. NASA National Snow and Ice Data Center*, doi: 10.5067/G519SHCKWQV6,

2015.

Kwok, R., and Cunningham, G. F.: Variability of Arctic sea ice thickness and volume from CryoSat-2, *Phil. Trans. R. Soc. A*, **373**(2045), 20140157, doi: 10.1098/rsta.2014.0157, 2015.

Kwok, R., and Markus, T.: Potential basin-scale estimates of Arctic snow depth with sea ice freeboards from CryoSat-2 and ICESat-2: An exploratory analysis, *Adv. Space Res.*, **62**(6), 1243–1250, doi: 10.1016/j.asr.2017.09.007, 2018.

Kwok, R., Kacimi, S., Webster, M. A., Kurtz, N. T., and Petty, A. A.: Arctic snow depth and sea ice thickness from ICESat-2 and CryoSat-2 freeboards: A first examination, *J. Geophys. Res.-Oceans*, **125**, e2019JC016008, doi: 10.1029/2019JC016008, 2020.

Kwok, R., Kurtz, N. T., Brucker, L., et al.: Intercomparison of snow depth retrievals over Arctic sea ice from radar data acquired by Operation IceBridge, *The Cryosphere*, **11**, 2571-2593, doi: 10.5194/tc-11-2571-2017, 2017.

Lang, A., Yang, S., and Kaas, E.: Sea ice thickness and recent Arctic warming. *Geophys. Res. Lett.*, **44**, 409-418, doi: 10.1002/2016GL071274, 2017.

Lawrence, I. R., Tsamados, M. C., Stroeve, J. C., Armitage, T. W. K., and Ridout, A. L.: Estimating snow depth over Arctic sea ice from calibrated dual-frequency radar freeboards, *The Cryosphere*, **12**, 3551–3564, doi:10.5194/tc-12-3551-2018, 2018.

Ledley, T. S.: Snow on sea ice: Competing effects in shaping climate, *J. Geophys. Res.-Atoms.*, **96**(D9), 17195-17208, doi: 10.1029/91JD01439, 1991.

Lee, S.-M., Meier, W. N., Sohn, B.-J., Shi, H., and Gaskiewski, A. J.: Estimation of Arctic Basin-Scale Sea Ice Thickness from Satellite Passive Microwave Measurements, *IEEE Trans. Geosci. Remote Sens.*, doi: 10.1109/TGRS.2020.3026949, 2021.

Lee, S.-M., and Sohn B.-J.: Retrieving the refractive index, emissivity, and surface temperature of polar sea ice from 6.9 GHz microwave measurements: A theoretical development, *J. Geophys. Res.-Atmos.*, **120**, 2293-2305, 2015.

Lee, S.-M., Sohn, B.-J., and Kim, S.-J.: Differentiating between first-year and multiyear sea ice in the Arctic using microwave-retrieved ice emissivities, *J. Geophys. Res.-Atmos.*, **122**, 5097-5112, doi: 10.1002/2016JD026275, 2017.

Lee, S.-M., Sohn, B.-J., and Shi, H.: Impact of ice surface and volume scatterings on the microwave sea ice apparent emissivity, *J. Geophys. Res.-Atmos.*, **123**, 9920-9237, doi: 10.1029/2018JD028688, 2018.

Liston, G. E., Itkin, P., Stroeve, J., Tschudi, M., Stewart, J. S., Pedersen, S. H., et al.: A Lagrangian snow-evolution system for sea-ice applications (SnowModel-LG): Part I—Model description, *J. Geophys. Res.-Oceans*, **125**, e2019JC015913. doi: 10.1029/2019JC015913, 2020.

Maaß, N., Kaleschke, L., Tian-Kunze, X., and Drusch, M.: Snow thickness retrieval over thick Arctic sea ice using SMOS satellite data, *The Cryosphere*, **7**(6), 1971–1989, doi: 10.5194/tc-7-1971-2013, 2013.

Markus, T., and Cavalieri, D. J.: Snow depth distribution over sea ice in the Southern Ocean from satellite passive microwave data, *Antarct. Res. Ser.*, **74**, 19–39, 1998.

Markus, T., Stroeve, J. C., and Miller, J.: Recent changes in Arctic sea ice melt onset, freezeup, and melt season length, *J. Geophys. Res.*, **114**, C12024, doi: 10.1029/2009JC005436, 2009.

Markus, T., et al.: The Ice, Cloud, and land Elevation Satellite-2 (ICESat-2): Science requirements, concept, and implementation, *Remote Sens. Environ*., **190**, 260–273, doi: 10.1016/j.rse.2016.12.029, 2017.

Masunaga, H. et al.: Satellite data simulation unit: A multisensory, multispectral satellite simulator package, *Bull. Am. Meteorol. Soc.*, **91**, 1625-1632, 2010.

Maykut, G. A., and Untersteiner, N.: Some results from a time-dependent thermodynamic model of sea ice, *J. Geophys. Res.*, **76**(6), 1550–1575, doi: 10.1029/JC076i006p01550, 1971.

Meier, W. N., Fetterer, F., Savoie, M., Mallory, S., Duerr, R., and Stroeve, J.: NOAA/NSIDC Climate Data Record of Passive Microwave Sea Ice Concentration, Version 3, *Boulder, Colorado USA, NSIDC: National Snow and Ice Data Center*, doi: 10.7265/N59P2ZTG, 2017a.

Meier, W. N., Fetterer, F., and Windnagel, A. K.: Near-Real-Time NOAA/NSIDC Climate Data Record of Passive Microwave Sea Ice Concentration, Version 1, *Boulder, Colorado USA, NASA National Snow and Ice Data Center Distributed Active Archive Center*, doi: 10.7265/N5FF3QJ6, 2017b.

Moore, G. W. K., Schweiger, A., Zhang, J., and Steele, M.: Collapse of the 2017 winter Beaufort high: A response to thinning sea ice?, *Geophys. Res. Lett.*, **45**(6), 2860-2869, doi: 10.1002/2017GL076446, 2018.

Nandan, V., Geldsetzer, T., Yackel, J., Mahmud, M., Scharien, R., Howell, S., King,

J., Ricker, R., and Else, B.: Effect of Snow Salinity on CryoSat-2 Arctic First-Year Sea Ice Freeboard Measurements, *Geophys. Res. Lett.*, **44**(20), 10,419–10,426, doi:10.1002/2017GL074506, 2017.

Perovich, D. K., Elder, B. C., and Richter-Menge, J. A.: Observations of the annual cycle of sea ice temperature and mass balance, *Geophys. Res. Lett.*, **24**(5), 555-558, 1997.

Perovich, D., Richter-Menge, J., and Polashenski, C.: Observing and understanding climate change: Monitoring the mass balance, motion, and thickness of Arctic sea ice, CRREL-Dartmouth mass balance buoy program, 2019. (available at http://imb-crrel-dartmouth.org, last accessed: September 2019)

Perovich, D., Richter-Menge, J., Tucker, W., Elder, B., and Bosworth, B.: Snow and Ice Temperature Profiles, Version 1.0. UCAR/NCAR – Earth Observing Laboratory, https://doi.org/10.5065/D6KS6PZ7, 2007.

Petty, A. A., Kwok, R., Bagnardi, M., Ivanoff, A., Kurtz, N., Lee, J., Wimert, J., and Hancock, D.: ATLAS/ICESat-2 L3B Daily and Monthly Gridded Sea Ice Freeboard, Version 1, *Boulder, Colorado USA, NASA National Snow and Ice Data Center Distributed Active Archive Center*, doi: 10.5067/ATLAS/ATL20.001, 2020.

Polashenski, C., Perovich, D., Richter-Menge, J., and Elder, B.: Seasonal ice mass-balance buoys: Adapting tools to the changing Arctic, *Ann. Glaciol.,* ***52***(57), 18-26, doi:10.3189/172756411795931516, 2011.

Ricker, R., Hendricks, S., Helm, V., Skourup, H., and Davidson, M.: Sensitivity of CryoSat-2 Arctic sea-ice freeboard and thickness on radar-waveform

interpretation, *The Cryosphere*, **8**, 1607–1622, doi: 10.5194/tc-8-1607-2014, 2014.

Rigor, I. G., and Wallace, J. M.: Variations in the age of Arctic sea-ice and summer sea-ice extent, *Geophys. Res. Lett.*, **31**(9), L09401, doi: 10.1029/2004GL019492, 2004.

Rigor, I. G., Wallace, J. M., and Colony, R, L.: Response of sea ice to the Arctic oscillation, *J. Clim.*, **15**(18), 2648-2663, doi: 10.1175/1520-0442(2002)015<2648:ROSITT>2.0.CO;2, 2002.

Rostosky, P., Spreen, G., Farrell, S. L., Frost, T., Heygster, G., and Melsheimer, C.: Snow depth retrieval on Arctic sea ice from passive microwave radiometers – improvements and extensions to multiyear ice using lower frequencies, *J. Geophys. Res.-Oceans*, **123**(10), 7120–7138, doi: 10.1029/2018JC014028, 2018.

Sallila, H., Farrell, S. L., McCurry, J., and Rinne, E.: Assessment of contemporary satellite sea ice thickness products for Arctic sea ice, *The Cryosphere*, **13**(4), 1187-1213. doi: 10.5194/tc-13-1187-2019, 2019.

Schluessel, P., and Luthardt, H.: Surface wind speeds over the North Sea from special sensor microwave/imager observations, *J. Geophys. Res.*, **96**(C3), 4845-4853. doi: 10.1029/90JC02493, 1991.

Screen, J. A., and Simmonds, I.: The central role of diminishing sea ice in recent Arctic temperature amplification, *Nature*, **464**, 1334-1337, 2010.

Serreze, M. C., Barrett, A. P., and Stroeve, J.: Recent changes in tropospheric water vapor over the Arctic as assessed from radiosondes and atmospheric

reanalyses, *J. Geophys. Res.-Atmos.*, **117**, D10104. doi: 10.1029/2011JD017421, 2012.

Serreze, M. C., and Barry, R. G.: Processes and impacts of Arctic amplification: A research synthesis, *Global Planet. Change*, **77**, 85-96, 2011.

Shalina, E. V. and Sandven, S.: Snow depth on Arctic sea ice from historical in situ data, *The Cryosphere*, **12**, 1867–1886, doi: 10.5194/tc-12-1867-2018, 2018.

Shi, H., Sohn, B.-J., Dybkjær, G., Tonboe, R. T., and Lee, S.-M.: Simultaneous estimation of wintertime sea ice thickness and snow depth from space-borne freeboard measurements, *The Cryosphere*, **14**, 3761-3783, doi: 10.5194/tc-14-3761-2020, 2020.

Stroeve, J., Liston, G. E., Buzzard, S., Zhou, L., Mallett, R., Barrett, A., et al.: A Lagrangian snow evolution system for sea ice applications (SnowModel-LG): Part II—Analyses, *J. Geophys. Res.-Oceans*, **125**(10), doi: 10.1029/2019JC015900, 2020.

Sturm, M., Holmgren, J., König, M., and Morris, K.: The thermal conductivity of seasonal snow, *J. Glaciol.*, **43**(143), 26–41, doi: 10.3189/S0022143000002781, 1997.

Sturm, M., Perovich, D. K., and Holmgren, J.: Thermal conductivity and heat transfer through the snow on the ice of the Beaufort Sea, *J. Geophys. Res.*, **107**(C21), 8043, doi: 10.1029/2000JC000409, 2002.

Tachibana, Y., Komatsu, K. K., Alexeev, V. A., Cai, L. and Ando, Y.: Warm hole in Pacific Arctic sea ice cover forced mid-latitude Northern Hemisphere cooling during winter 2017-18, *Sci. Rep.*, **9**, 5567, doi: 10.1038/s41598-019-

41682-4, 2019.

Timco, G. W, and Frederking, R. M. W.: A review of sea ice density, *Cold Reg. Sci. Technol.*, 24, 1-6, 1996.

Tonboe, R. T., Pedersen, L. T., Haas, C.: Simulation of the CryoSat-2 satellite radar altimeter sea ice thickness retrieval uncertainty, *Can. J. Remote Sens.*, **36**(1), 55–67, doi: 10.5589/m10-027, 2010.

Tschudi, M., Meier, W. N., Stewart, J. S., Fowler, C., and Maslanik, J.: EASE-Grid Sea Ice Age, Version 4, *Boulder, Colorado USA. NASA National Snow and Ice Data Center Distributed Active Archive Center*, doi: 10.5067/UTAV7490FEPB, 2019a.

Tschudi, M., Meier, W. N., Stewart, J. S., Fowler, C., and Maslanik, J.: Polar Pathfinder Daily 25 km EASE-Grid Sea Ice Motion Vectors, Version 4, *Boulder, CO, NASA National Snow and Ice Data Center Distributed Active Archive Center*, doi: 10.5067/INAWUWO7QH7B, 2019b.

Ulaby, F. T., Moore, R. K., and Fung, A. K.: Microwave remote sensing: Active and passive, Volume 3 - From theory to applications, 1986.

Untersteiner, N.: Natural desalination and equilibrium salinity profile of perennial sea ice, *J. Geophys. Res.*, 73(4), 1251-1257, doi: https://doi.org/10.1029/JB073i004p01251.

Vant, M. R., Ramseier, R. O., and Makios, V.: The complex dielectric constant of sea ice at frequencies in the range 0.1-40 GHz, *J. Appl. Phys.*, **49**(3), 1264-1280, 1978.

Wang, C., Graham, R. M., Wang, K., Gerland, S., and Granskog, M. A.:

Comparison of ERA5 and ERA-Interim near-surface air temperature, snowfall and precipitation over Arctic sea ice: effects on sea ice thermodynamics and evolution, *The Cryosphere*, **13**, 1661–1679, doi:10.5194/tc-13-1661-2019, 2019.

Warren, S. G., and Brandt, R. E.: Optical constant of ice from the ultraviolet to the microwave: A revised compilation, *J. Geophys. Res.*, **113**(D14), D14220, doi: 10.1029/2007JD009744, 2008.

Warren, S. G., Rigor, I. G., Untersteiner, N., Radionov, V. F., Bryazgin, N. N., Aleksandrov, Y. I., and Colony, R.: Snow depth on Arctic sea ice, *J. Climate*, **12**(6), 1814–1829, doi: 10.1175/1520-0442(1999)012<1814:SDOASI>2.0.CO;2, 1999.

Webster, M. A., Rigor, I. G., Nghiem, S. V., Kurtz, N. T., Farrell, S. L., Perovich, D. K., and Sturm, M.: Interdecadal changes in snow depth on Arctic sea ice, *J. Geophys. Res.-Oceans*, **119**(8), 5395–5406, doi: 10.1002/2014JC009985, 2014.

Webster, M. A., Parker, C., Boisvert, L., and Kwok, R.: The role of cyclone activity in snow accumulation on Arctic sea ice, *Nat. Commun.*, **10**, 5285, doi: 10.1038/s41467-019-13299-8, 2019.

Wingham, D. J., et al.: CryoSat: a mission to determine the fluctuations in Earth's land and marine ice fields, *Adv. Space Res.*, **37**(4), 841–871, doi: 10.1016/j.asr.2005.07.027, 2006.

Willatt, R., Laxon, S., Giles, K., Cullen, R., Haas, C., and Helm, V.: Ku-band radar penetration into snow cover on Arctic sea ice using airborne data, *Ann. Glaciol.*, **52**, 197–205, doi:10.3189/172756411795931589, 2011.

Yeo, H., Park, S.-J., Kim, B.-M., Shiobara, M., Kim, S.-W., Kwon, H., Kim, J.-H., Jeong, J.-H., Park, S. S., and Choi, T. J.: The observed relationship of cloud to surface longwave radiation and air temperature at Ny-Ålesund, Svalbard, *Tellus B*, **70**(1), doi: 10.1080/16000889.2018.1450589, 2018.

Yi, D., and Zwally, H. J.: Arctic Sea Ice Freeboard and Thickness, Version 1, *Boulder, Colorado USA, NASA National Snow and Ice Data Center Distributed Active Archive Center*, doi: 10.5067/SXJVJ3A2XIZT, 2009.

Zhou, L., Stroeve, J., Xu, S., Petty, A. et al.: Inter-comparison of snow depth over Arctic sea ice from reanalysis reconstructions and satellite retrieval, *The Cryosphere*, **15**, 345-367. doi: 10.5194/tc-15-345-2021, 2021.

Zhou, L., Xu, S., Liu, J., and Wang, B.: On the retrieval of sea ice thickness and snow depth using concurrent laser altimetry and L-band remote sensing data, *The Cryosphere*, **12**(3), 993–1012, doi: 10.5194/tc-12-993-2018, 2018.

Zygmuntowska, M., Rampal, P., Ivanova, N., and Smedsrud, L. H.: Uncertainties in Arctic sea ice thickness and volume: new estimates and implications for trends, *The Cryosphere*, **8**, 705–720, doi: 10.5194/tc-8-705-2014, 2014.

Zwally, H. J., Schutz, B., Abdalati, W., Abshire, J., Bentley, C., Brenner, A., Bufton, J., Dezio, J., Hancock, D., Harding, D., Herring, T., Minster, B., Quinn, K., Palm, S., Spinhirne, J., and Thomas, R.: ICESat's laser measurements of polar ice, atmosphere, ocean, and land, *J. Geodyn.*, **34**, 405–445, doi: 10.1016/S0264-3707(02)00042-X, 2002.

국문 초록

겨울철 북극 해빙지역 적설깊이 산출을 위해 적설-해빙 시스템의 정역학적 평형 및 열역학적 정상상태(steady state)를 기반으로 한 새로운 인공위성 산출 알고리즘이 개발되었다. 개발된 알고리즘은 수동 마이크로파/적외선 관측자료로부터 얻어진 해빙건현(freeboard), 적설표면온도와 적설-해빙 경계층온도를 입력자료로 사용하여 적설깊이 산출을 수행한다. 적설깊이 산출물은 NASA의 OIB(Operation IceBridge) 항공기 관측자료를 기준으로 검증되었으며 높은 정확도를 보였다. 새로운 알고리즘을 활용한 북극해 규모의 장기간 적설깊이 자료 생산을 위해 인공위성 수동 마이크로파 관측자료로부터 해빙건현을 추정하였다. 이를 위해 수동 마이크로파 관측에서 얻은 적설-해빙 산란 광학 깊이를 예측 변수로 사용하였다. 추정된 수동 마이크로파 해빙건현은 OIB 관측치와 높은 일치성을 보였다.

2003-2020년 기간 겨울철 적설깊이 자료를 인공위성 온도자료와 수동 마이크로파 해빙건현자료를 함께 사용하여 생산하고 분석하였다. 북극 해빙지역 적설깊이는 눈이 쌓이는 시기 및 기간과 관련하여 해빙의 종류에 크게 의존하는 것으로 나타났으며, 적설깊이와 그 변동성은 단년빙보다 다년빙에서 큰 값을 보였다. 또한, 1954-1991년 기간 동안의 현장관측 기반 적설깊이 기후값과 비교하여 현대 적설깊이의 상당한 감소가 발견되었다. 시계열 분석 결과 2003-2020년 기간동안 지역적으로 다른 적설깊이 경향성이 보

였다. 북극해의 동쪽지역에서는 감소, 서쪽지역에서는 증가 경향이 나타났다. 감소 경향은 다년빙에서 단년빙으로의 해빙 종류 변화 및 결빙시점의 지연과 관련이 있으며, 증가 경향은 강수량의 증가와 관련이 있는 것으로 보인다.

주요어: 적설깊이, 북극 해빙, 인공위성 원격탐사, 기후변화

학 번: 2016-29111